



**Chapter 3: Detailed Studies of Nickel Schiff-base
Complexes Encapsulated in Zeolite Y**



Chapter 3: Part A

Encapsulation of Ni Salen Complex in Zeolite Y:

An Experimental and DFT Study

3A.1. INTRODUCTION

Zeolites the micro porous aluminosilicate materials with cavities and channels of specific architectures have been extensively investigated for encapsulation of transition metal complexes, other organometallics, and polymers. Encapsulation provides a fascinating way of coupling the reactivity of the metal complex with the robustness and stereochemistry of the host zeolite framework,¹⁻⁶ which is nothing but an alternative route for the heterogenization of an otherwise homogeneous catalyst, with additional advantages like shape selectivity, site isolation, easy separation, resistivity at higher temperatures and better reactivity.⁷⁻¹¹ These hybrid catalysts have wide range of applications in gas purification, catalysis and biomimetic chemistry.¹¹⁻¹³ A fascinating subgroup of such encapsulated complexes are “ship-in-a-bottle” complexes, where building blocks of the complex are assembled together in the cavity of the porous solid and once synthesized, due to its size, the complex cannot 'leak out' through the pores without destruction of the framework.¹⁴ It has already been well established that the space constraints imposed by the host framework can have profound influence on the structure of guest complex which can induce changes in magnetic, spectroscopic and redox properties of the encapsulated complex as compared to its properties in solution or in the solid-state leading to an enhanced reactivity or better selectivity from its solution state.¹⁴⁻¹⁸ The catalytic activity of the encapsulated Schiff base complexes are well identified, they are potential heterogeneous catalyst for oxidation/epoxidation of alkanes, alkenes¹⁹⁻²² and alcohols²³ with range of oxidants, *e.g.* tertbutylhydroperoxide (TBHP), hydrogen peroxide (H₂O₂), and molecular O₂. P. Ratnasamy *et al* have reported that encapsulated copper salen and 5-chloro copper salen complexes in zeolite Y are efficient catalysts for oxidation of p-xylene, phenol and decomposition of TBHP and H₂O₂.²⁴ Recently, Deka *et al* have reported that encapsulated complex of Fe(III)-Schiff-base in zeolite Y is efficient catalyst for oxidative coupling of 2-naphthol²⁵ and encapsulated complex of copper(II) salen in zeolite-Y shows enantioselectivity for Henry Reaction.²⁶ Phthalocyanine, porphyrine and salen complexes in zeolite Y are well known biomimetic systems and have the functional analogy with cytochrome P-450.^{12, 13, 27} The encapsulation of FePc in zeolite-Y yields a catalyst which shows 10³ times more activity for the oxidation of alkanes as compared to the its 'neat' form in solution.¹⁵ It is quite evident that the topology of the zeolite framework could have significant influence on the geometry of the guest molecule, which in turn could be correlated

with the modified functionality of the system in terms of reactivity and selectivity. Relatively lesser number of reports are existing in the literature exploring these aspects. Notably, Mizano *et al* have reported a novel temperature driven inter-conversion between a low-spin and a high-spin state of cobalt(II)tris(bipyridyl) complex encapsulated in zeolite Y.¹⁷ Magnetic and spectroscopic studies of the $[\text{Co}(\text{bpy})_3]^{2+}$ complex reveals that it adopts an octahedral geometry under encapsulation which is less distorted as compared to its “free” state.²⁸ Mössbauer and optical spectroscopic studies of 6 coordinated Fe^{2+} complexes with a series of ligands have revealed that the complex of comparable size with that of the zeolite cavity undergoes trigonal prismatic distortion from octahedral geometry on encapsulation, whereas smaller complex doesn’t show any such distortion.²⁹ A detailed study of Co phthalocyanine complex in “free” and encapsulated in zeolite-Y and MCM-41 had been carried out by Ray *et al*,³⁰ and it is observed that the encapsulated complex undergoes a saddle type distortion from planarity and the change in symmetry after encapsulation affects its magnetic behavior and shows enhanced magnetic moment than “neat” CoPc complex. Similar studies on $[\text{Ni}^{\text{II}}\{\text{salnptn}(4\text{-OH})_2\}]$ complex, indicate that the complex undergoes distortion under the influence of a constrained zeolite framework thus influencing the electronic structure of the molecular system.³¹

In the present study, we report the synthesis of encapsulated NiL3, [L3: *N,N*-bis(5-hydroxy-salicylidene)ethylenediamine] complex *via* flexible ligand synthesis method inside the zeolite Y (given in scheme 3A.1) and also in MCM-41. A detailed chemical, morphological and surface studies (XRD, SEM) along with spectroscopic (FTIR, UV-Vis) and magnetic studies of the encapsulated complex and the isolated complex are carried out. The observed shift in UV-Vis spectra as well as a drastic change in magnetic moment (diamagnetic when free and paramagnetic when encapsulated in zeolite) of the guest complex within the zeolite pore indicates that the geometry does not remain planar around the Ni centre. Theoretical studies of the geometry and electronic structure of NiL3 complexes in different spin states are also carried out in free and encapsulated state using Density Functional Theory (DFT) for better understanding of the structure adopted by the complex and corresponding evaluation of the magnetic moment while entrapped within zeolite Y. Using TD-DFT methods we have simulated the UV-Vis spectra of the complex which helps in understanding the nature of the

spectral transitions in the light of deformation of the square-planar guest complex upon encapsulation.

3A.2. RESULTS AND DISCUSSION

Synthesis of ligand, complex in free as well as encapsulated state is already discussed in chapter 2 under experimental section 2.2.1-2.27.

3A.2.1. X-ray Powder Diffraction Studies

To ensure the preservation of zeolite framework integrity, as well as encapsulation of guest complex inside the cavity of the host, powder X-rays diffraction patterns of pure zeolite Y, Ni-exchanged Y, and encapsulated complex NiL3 are recorded (Shown in Figure 3A.1). Essentially similar XRD patterns of these systems indicate the retention of integrity of zeolite framework during the encapsulation and even after the complex formation.

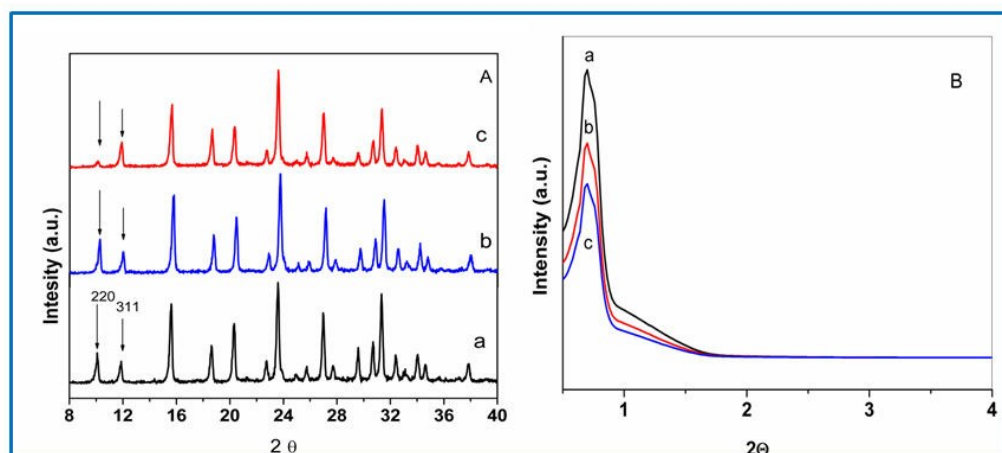


Figure 3A.1: (A) Powder XRD pattern of (a) pure zeolite-Y, (b) Ni exchanged zeolite-Y, (c) Encapsulated NiL3 in zeolite Y, (B) The XRD patterns of (a) Al-MCM-41, (b) Ni-Al-MCM-41 and (c) Encapsulated NiL3 in MCM-41 at the range of ($0 < 2\theta < 4$).

A noticeable difference in the XRD patterns of zeolite Y with encapsulated complex from that of zeolite Y is an alternation in the relative intensities of peak positions of the 220 and 311 reflections (I_{220} and I_{311} respectively) appearing at $2\theta = 10^\circ$ and 12° , respectively. For pure zeolite and Ni-exchanged zeolite the relation $I_{220} > I_{311}$ holds, but for zeolite with encapsulated complex it is observed as $I_{311} > I_{220}$. This intensity reversal has already been identified and empirically correlated with the presence of a large complex within the zeolite-

Y supercage.^{32, 33} The above study may suggest the presence of a large NiL3 complex inside the cavity of zeolite framework. No alternation of the peak intensities is observed for the complex formation occurring on the surface.^{23,37} This change in the relative intensities may be associated with the rearrangement of randomly coordinated free cations in zeolite Y at different sites.³¹ The above observations indicates successful encapsulation NiL3 complex within void of the supercage Y.

The XRD patterns of Al-MCM-41, Ni-Al-MCM-41 and encapsulated NiL3 in MCM-41 are shown in Figure 3A.1. All three samples show very intense peak at $2\theta = 0.68 - 0.70$, that is indexed to 100 plane, the high intensity of 100 plane peak shows high degree of long-range order and existence of uniform pores in the synthesized material.³⁴⁻³⁶ Additional unresolved broader area is identified due to 110 and 200 planes. There is no further modification detected in nickel exchanged and encapsulated complex in MCM-41 XRD patterns, which clearly indicates the integrity of the MCM framework during the metal exchange and even encapsulation processes.

3A.2.2. Elemental Analysis

The unit cell formula of the parent sodium zeolite Y is $\text{Na}_{58}\text{Al}_{58}\text{Si}_{136}\text{O}_{388}\cdot y\text{H}_2\text{O}$. and Si/Al ratio is 2.34. EDX data indicate the unaffected Si/Al ratio even after exchange and encapsulation reactions. It signifies that the dealumination doesn't take place during encapsulation processes. The metal concentration in encapsulated complex is found to be lesser than ion exchanged zeolite Y, which directs towards the fact of participation of metal ions in coordination inside the cavities. Another possibility may be the leaching of some metal ions during the complex formation which causes the reduction metal-ion concentration. The general formula of Ni-exchanged zeolite-Y sample is $\text{Ni}_x\text{Na}_{58-2x}\text{Al}_{58}\text{Si}_{136}\text{O}_{388}\cdot y\text{H}_2\text{O}$. From AAS studies x is found to vary within 2 to 4. In the encapsulated complex the concentration of nickel metal is found less than 1 (0.68) wt percentage.

3A.2.3. Scanning Electron Microscopy

Encapsulation of nickel salen complex in zeolite Y is accomplished *via* flexible ligand synthesis method, to synthesize 'Zeozymes' where formation of the complex is essentially targeted inside the cavities of supercage not on the surface of the host framework. But formation of complex only inside the cavities is practically not viable, because some of the

metal complexes can always be adsorbed on surface or some ligands may remain uncoordinated. To investigate surface morphology of zeolite Y specifically after encapsulation, SE micrographs of encapsulated NiL3 complex in zeolite Y before and after soxhlet extraction (Figure 3A.2) are analyzed and SEM images indicate, before extractions there are some visible surface species in the form of complexes or un-reacted ligands but are absent after extraction.^{25, 31} The particle boundaries on the external surface are clearly visible due to the complete removal of deposited adsorbed species on the surface in final product. The color of Soxhlet extracted final product definitely is a sign of successful encapsulation of the complex inside the cavities of zeolite.

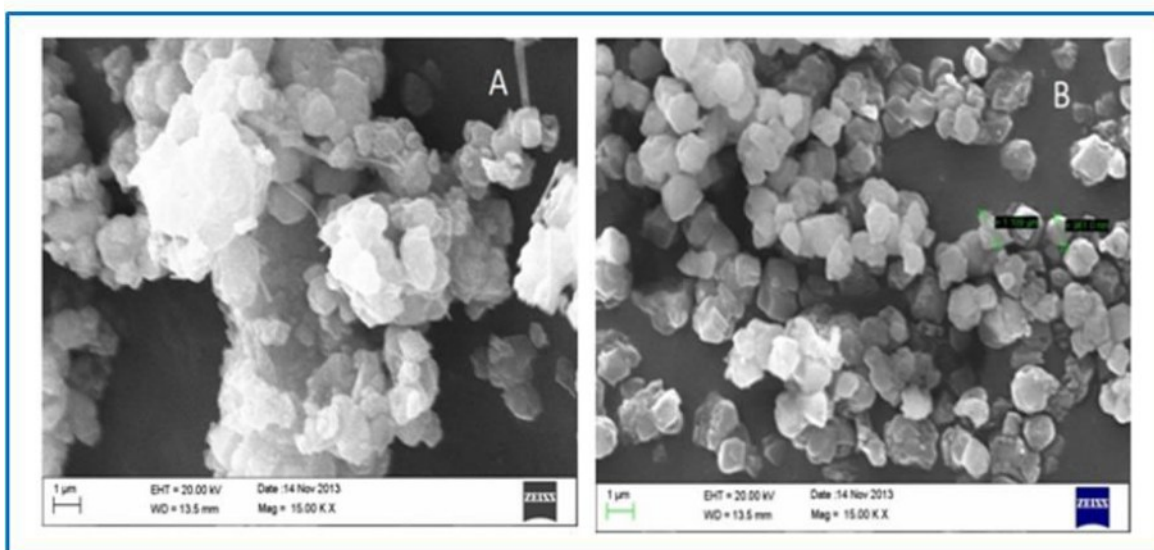


Figure 3A.2: SE micrograph of encapsulated NiL3 in zeolite Y, (A) before Soxhlet extraction, (B) after Soxhlet extraction.

3A.2.4. Infrared Spectroscopy

The FTIR spectra of Na-zeolite-Y, encapsulated NiL3 in zeolite-Y are shown in Figure 3A.3. IR spectrum of Na-zeolite-Y shows major bands in $450\text{--}1200\text{ cm}^{-1}$ region with additional bands at 1643 cm^{-1} and 3500 cm^{-1} region. The major characteristics bands at $560, 717, 786,$ and 1018 cm^{-1} are attributed to $(\text{Si}/\text{Al}-\text{O})_4$ bending mode, double ring, symmetric stretching, asymmetric stretching vibration, respectively.^{25, 37} The broad bands observed at 3500 cm^{-1} and 1643 cm^{-1} are due to surface hydroxylic group and lattice water molecules respectively.^{31, 38} These bands are not significantly altered after the ion exchange and even after encapsulation of the complex inside the supercage, (indicated by asterisk in Figure 3A.3).

This observation definitely suggests that the zeolite framework is remaining unaffected after encapsulation process. The characterization of encapsulated complex is somewhat difficult by IR spectroscopy because the intensity of IR bands of encapsulated complexes are very weak due to low concentration of complex inside the framework and zeolite bands interfere in proper observation of the complex. The region of 1200-1600 cm^{-1} is appropriate to study because in this region, zeolite bands are almost silent and some of the prominent bands of the complex appear in this region with little shift in the peak positions. The expanded IR spectra (in range of 600-2000 cm^{-1}) are shown in Figure 3A.3. The lower shift in the case of (C=N) and (C-O) stretching frequencies identify nitrogen and oxygen coordination inside the cavity of the zeolite framework.³⁹ The $\nu_{\text{C-H}}$ deformation bands at 1382 cm^{-1} in case of encapsulated complex, are shifted towards higher wavenumbers, which indicate the encapsulation of the nickel Schiff-base complex inside the zeolite-Y.⁴⁰ The observed FTIR spectral data (Table 3A.1) suggest the formation of a nickel Schiff-base complex in the ‘free’ as well as encapsulated state inside the supercage of zeolite.

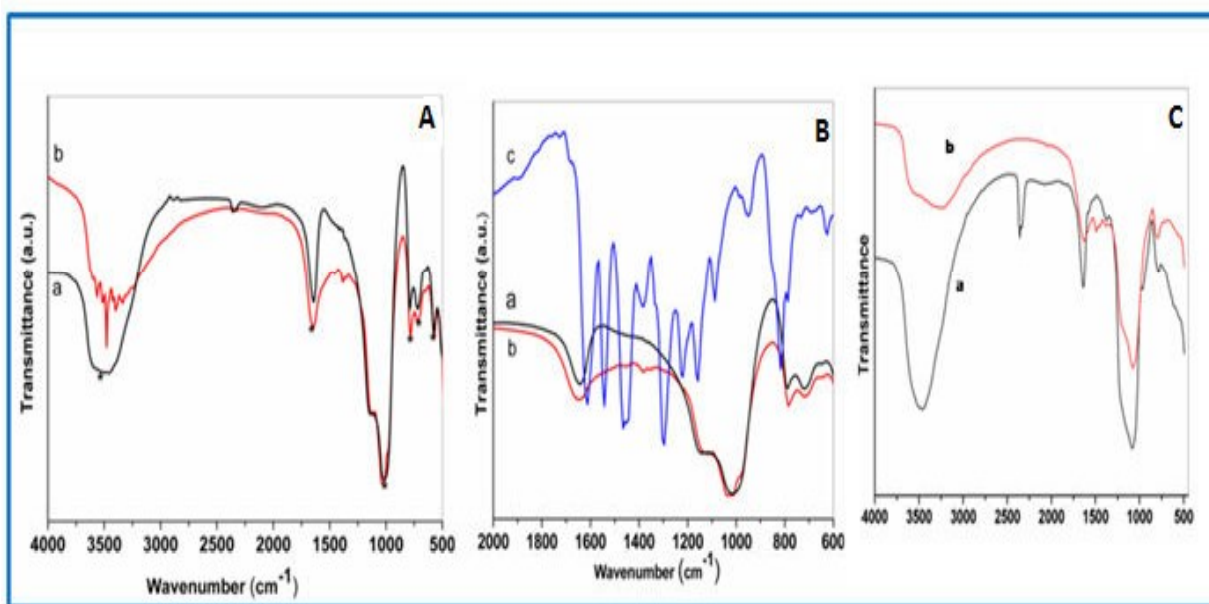


Figure 3A.3: (A) FTIR spectra in the range of 500 cm^{-1} to 4000 cm^{-1} of (a) pure zeolite Y, (b) encapsulated NiL3 in zeolite Y (B) The FTIR spectra in the range of 600 cm^{-1} to 2000 cm^{-1} (a) pure zeolite Y, (b) encapsulated NiL3 in zeolite Y, (c) ‘neat’ NiL3 complex. (C) FTIR spectra in the range of 500 cm^{-1} to 4000 cm^{-1} of (a) pure MCM-41, (b) encapsulated NiL3 in MCM-41

Table 3A.1: FTIR spectral data (in cm^{-1}) for the “neat” and encapsulated NiL3 complex.

S.No	Sample	(C=N stretching)	(C=C stretching)	($\nu_{\text{C-H}}$ deformation)	(C-O stretching)
1.	L3	1635	1580,1481	1381	1352
2.	NiL3	1620	1542, 1465	1375	1332
3.	NiL3 -Y	1642	1551, 1451	1382	1301
4.	NiL3 - MCM-41	1631	1495, 1450	1391	merged

3A.2.5. Theoretical Studies & Results

To have the better insight of the hybrid host-guest system, the complex both in its neat and encapsulated forms are studied theoretically (details of methodology are mentioned in Chapter 2 in section 2.3.9 under theoretical methods). In the ground state the complex NiL3 is planar⁴¹⁻⁴³ and exists as singlet with no unpaired electrons. The structure of the Ni-salen complexes in free (neat) state and then in encapsulated form are optimized and the resulting structures are shown in Figure 3A.4. The geometrical parameters when compared with experimental XRD data show good agreement for the free complexes.⁴⁴ The isolated NiL3 studied is planar and is more stable in singlet state without any unpaired electrons, but can also exist as a higher energy triplet state with two unpaired electrons. The calculated energy difference between the triplet state and the singlet state for isolated NiL3 is 21.47 kcal. After encapsulation, however, the non planer triplet state is substantially stabilized, but still remains less stable than the singlet state by 8.1 kcal. Due to the modest difference in energies, the possibility of a reasonable fraction of the complex existing in triplet state after encapsulation cannot probably be ruled out. Calculated spin density on Ni atom is 1.54 (total moment: $2.35 \mu_{\text{B}} [n(n+2)^{1/2}]$) for the triplet NiL3. Apart from the ethylene linkage portion the singlet complexes are largely planar as appear in Figure 3A.4. We report few selected bond lengths and bond angles obtained from geometry optimizations for the free and the encapsulated complexes in Table 3A.2. It is seen that bond distances Ni-N and Ni-O of complex vary after encapsulation. The bond angles O-Ni-N and C-Ni-C also changes upon

encapsulation, bond angle C-Ni-C (marked in Figure 3A.4 as rectangular boxes) is actually a measure of the planarity of the molecule in free or encapsulated state. This angle is 179.9° for the free singlet molecule, but decreases for the encapsulated one, with a large decrease to 165.3° in case of singlet and even larger decrease to 160.48° in case of the triplet state. After encapsulation, the complexes are bent and distorted which is reflected in the changed bond-distances and angles. The extent of bending is also clear from the end-to-end distances shown in Table 3A.2, where the distance decreases from 14.3\AA to 13.7\AA (singlet) and 13.48\AA (triplet) when NiL3 is encapsulated in contrast to the free molecule. The change in the bond distances and bond angles on encapsulation may be attributed to the influence of the zeolite framework, where the topology of the supercage is expected to impose steric constraints on the complex.

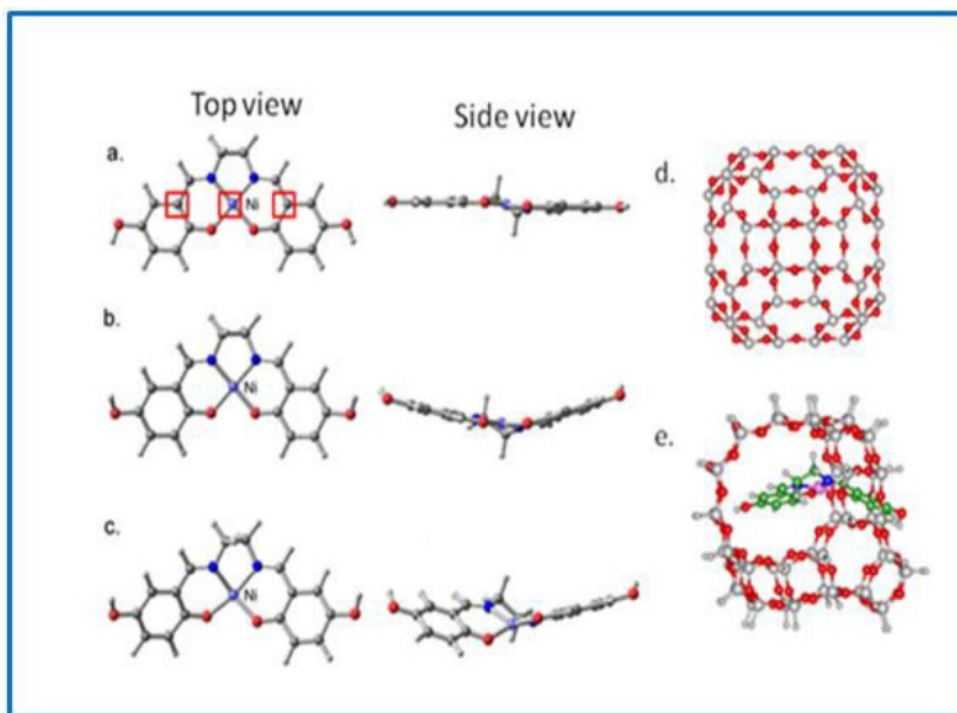


Figure 3A.4: (a) NiL3 molecule (singlet) free state (b) NiL3 molecule (singlet) is encapsulated and extracted (c) NiL3 molecule (triplet) is encapsulated and extracted. The atoms marked by the square define the C-Ni-C bond angle. (d) The zeolite framework used for theoretical studies (e) NiL3 molecule (triplet) is encapsulated within the zeolite pore. Closest non-bonding distance between NiL3 and the zeolite framework is $\sim 3.1\text{\AA}$.

Table 3A. 2: Important geometrical parameters and molecular orbital's for NiL3 in free and encapsulated case.

Bond distances(Å)/ angles(^o) /Energy (eV)	NiL3 free singlet	NiL3 encapsulated in zeolite Singlet	NiL3 encapsulated in zeolite Triplet
Ni-O (Å)	1.85	1.83	1.88
Ni-N (Å)	1.87	1.85	1.97
O-C (Å)	1.30	1.30	1.30
N-C(conj) (Å)	1.30	1.30	1.30
<O-Ni-N	94.0	93.2	92.22
<C-Ni-C	179.9	165.3	160.48
End to end distance (Å)	14.32	13.70	13.48
HOMO (eV)	-4.97	-5.03	-5.32, -5.46
LUMO(eV)	-1.86	-1.88	-1.93, -2.35
HOMO-LUMO gap (eV)	3.11	3.14	3.39, 3.11

The natures of the few important frontier molecular orbitals for the salen complexes as well as the optimized structures are presented in Figure 3A.5. In the free singlet molecule, the HOMO is mainly localized on p_z orbitals on N, O and C atoms along with d_{yz} on Ni which are responsible for a delocalized pi orbital. The LUMO mainly consists of p orbitals of O, N and C along with only a tiny contribution from Ni d_{xz} orbital. $HOMO^{-1}$ and $LUMO^{+1}$ orbitals are also primarily pi orbitals with only a small contribution from Ni d_{xz} for $HOMO^{-1}$ and almost no Ni contributions for $LUMO^{+1}$. $HOMO^{-2}$ is mostly localized on metal d_z^2 while $LUMO^{+2}$ is mostly localized on p and d_{xy} orbitals of Ni along with p orbitals of O and N. $HOMO^{-3}$ is mainly p and d_{xz} on Ni and p on N,O and C atoms. $LUMO^{+3}$ has no contributions from metal d orbital. The nature and the energies of the HOMO and LUMO for the free singlet complex and those extracted from zeolite are represented as a comparative energy

diagram in Figure 3A.4. This figure also shows how the MO energies change after encapsulation for NiL3 singlet state and we find only a modest change in MO energies, in spite of bending (Figure 3.A. 6). The molecular orbitals of the encapsulated triplet state of NiL3 is shown in Figure 3A.7 and these orbitals are very different from the MOs of the isolated singlet complex.. In this case there are alpha and beta type of orbitals for up-spin and down-spin electrons, and it is seen from the Figure 3A.7 that HOMO, HOMO⁻¹ and HOMO⁻² orbitals are contributed by Ni d orbitals and the C pi orbitals of salen. For the frontier unoccupied orbitals also Ni d contributes strongly along with C p orbitals *eg* LUMO, LUMO⁺¹ and LUMO⁺².

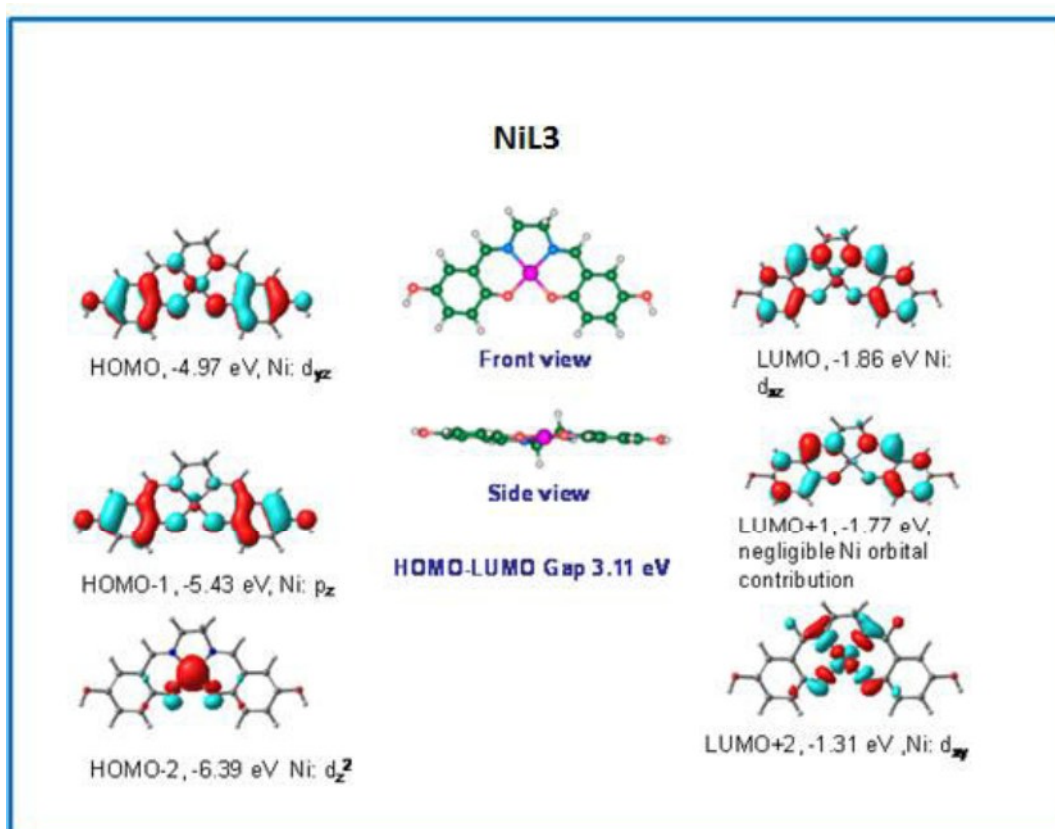


Figure 3A.5: The structure and important molecular orbitals for NiL3. The frontier orbitals with clear metal orbital characters are shown.

The singlet complex undergoes a considerable deviation from its planar geometry under encapsulation and the calculated gas phase TD-DFT spectrum of NiL3 complex both encapsulated (singlet) and encapsulated (triplet) are given in Figure 3A.8 a-b and the

corresponding transitions are shown in Table 3A.4. The nature of the spectra remains same for the isolated singlet and the encapsulated singlet cases but there are clear increase in transition energies and consequent decrease in wavelength of the first few transitions, namely isolated NiL3: 652.8 nm (1.90 eV), encapsulated NiL3 617.8 nm (2.01 eV); 559 nm (2.22 eV) and 532.6 nm (2.33 eV); 490.9 nm (2.53 eV) and 469.8 nm (2.64 eV) and few more with smaller shifts; all of which involves mainly the transition metal d orbitals.

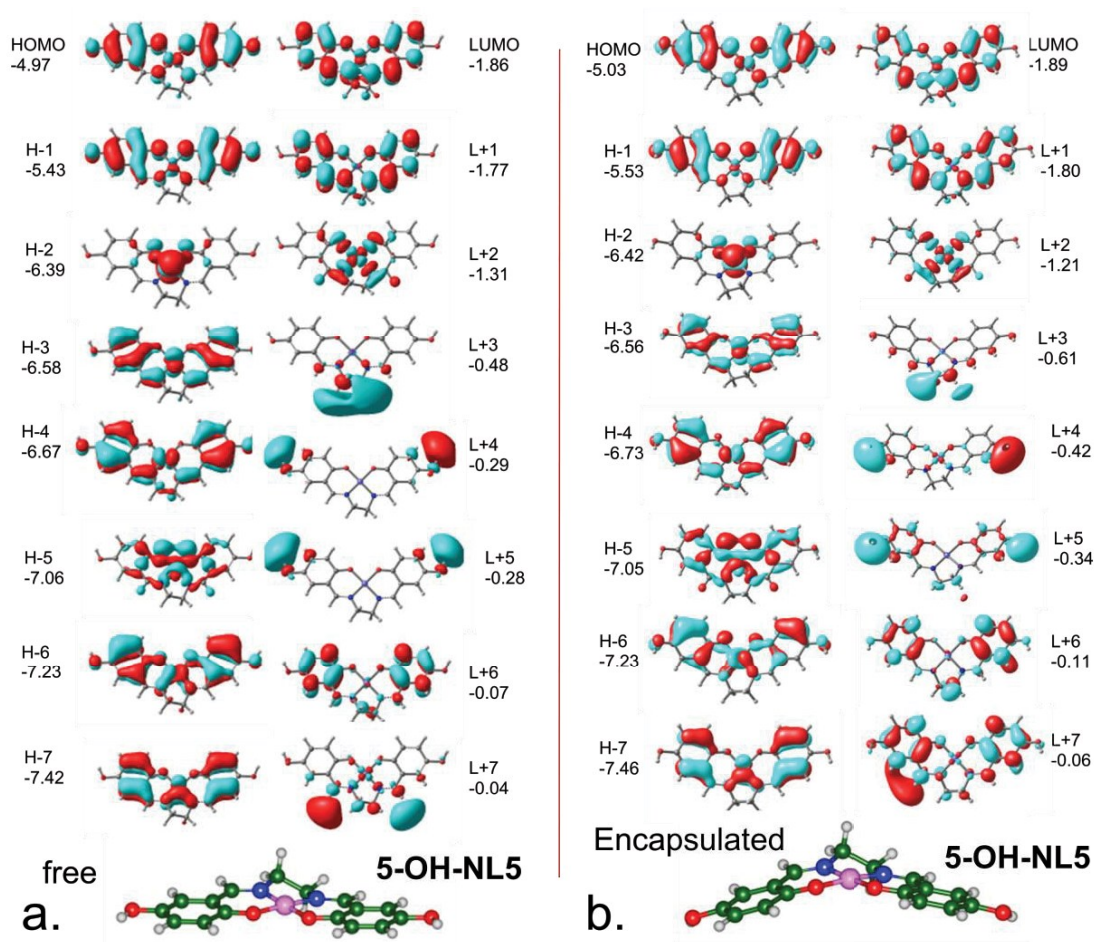


Figure 3A.6: (a) The molecular orbitals of NiL3 in free state, including the HOMO, LUMO. The orbitals lower in energy than HOMO are marked as H-n (n = 0 being HOMO) and LUMO+n (n = 0 being LUMO). (b) The molecular orbitals of NiL3 in encapsulated singlet state, including the HOMO, LUMO. Corresponding molecular structures are shown for reference.

The first transition at 652.8 nm occurs primarily due to transition from HOMO to LUMO⁺² which is a d-d transition and the peak at 559 nm is due to transition from HOMO⁻² to LUMO⁺² which is again a d-d transition. A fairly intense HOMO to LUMO transition is observed at 478 nm also involved Ni d orbitals. It is these transitions which are mostly affected when the molecule is encapsulated, and the d-d transitions are observed at lower wavelengths for the encapsulated molecule and above transitions occur at 617.8, 532.2 and 469.8 nm respectively for the encapsulated case.

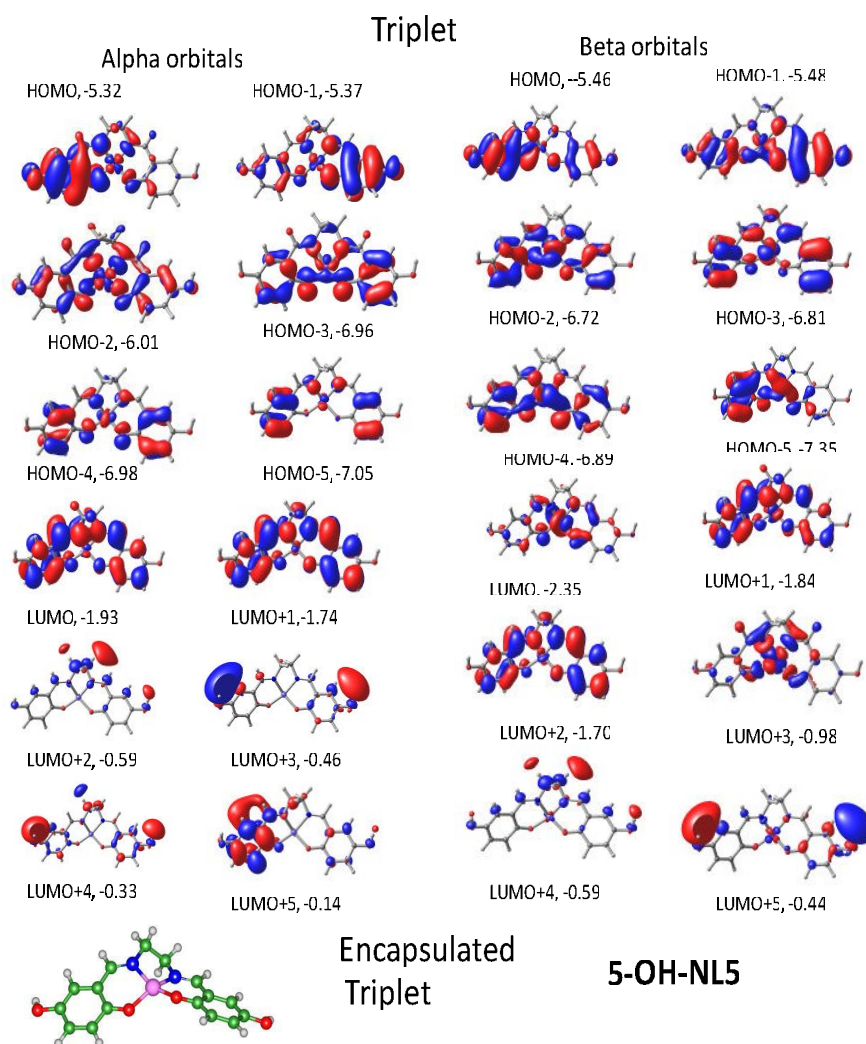


Figure 3A.7: The molecular orbitals of NiL3 in encapsulated triplet state, including the HOMO, LUMO. The orbitals lower in energy than HOMO are marked as HOMO-n (n = 0 being HOMO) and LUMO+n (n=0 being LUMO). Corresponding molecular structure is shown for reference.

When the TD-DFT spectrum of triplet NiL3 is considered we find that important d-d transitions occur at 594.6 (2.08 eV) and 540.6 nm (2.29 eV); of which the second one is reasonably intense in contrast to the isolated singlet case. Analysis of the spectral transitions and molecular orbitals (Figure 3A.7) shows that the peak at 594.6 nm is due to transitions from HOMO to LUMO along with $LUMO^{+1}$, $HOMO^{-1}$ to LUMO and $HOMO^{-2}$ to $LUMO^{+2}$. The intense peak at 540.6 nm is primarily due to transitions from HOMO to LUMO and $LUMO^{+1}$. However, the analysis of the transitions become difficult in case of triplet complex, as the orbitals become more hybridized with ligand orbitals due to strong distortion.

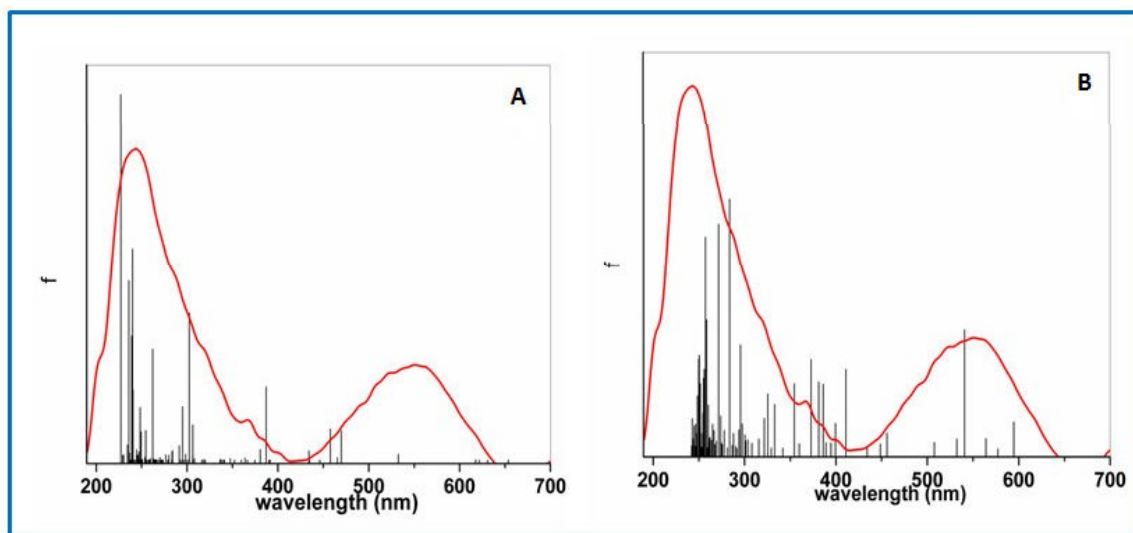


Figure 3A.8: Experimental and DFT simulated UV-Vis spectra of (A) DFT simulated singlet state (black vertical graph) and experimental encapsulated NiL3 in zeolite Y, (red line graph) (B) DFT simulated triplet state (black vertical graph) and experimental encapsulated NiL3 in zeolite Y, (red line graph).

Table 3A.3. UV-Vis experimental and TD-DFT simulated spectral data of the “neat” and encapsulated NiL3 in solid state with corresponding assignments.

(NiL3) in chloro form	solid state (NiL3)	DFT (NiL3) singlet	Transitions (singlet)	(Encapsulated NiL3 in zeolite Y) solid state	DFT (Encapsulated NiL3 in zeolite Y) singlet	Transitions (singlet)	DFT (Encapsulated NiL3 in zeolite Y) triplet	Transitions (triplet)
240 (258)	240 (s)	295	$H^{-2} \rightarrow L^0$	244	295	$H^{-5} - L^0$	257	$H^{-4} \rightarrow L^{+1}$ $H^0 \rightarrow L^{+5}$

Chapter 3A

sh)								
		301	H^3-L^{+1} H^5-L^0		302	H^3-L^{+1} H^5-L^0 H^4-L^0	271	H^4-L^0 H^3-L^0
328	332	351	H^0-L^{+2} H^2-L^0 H^4-L^{+2}	288	336	H^0-L^{+2} H^2-L^0 H^4-L^{+2}	283	H^4-L^{+2} H^6-L^{+2} H^3-L^{+2}
							295	H^1-L^{+2} H^5-L^{+1} H^3-L^{+1}
361		365	H^2-L^0 H^0-L^{+2} H^4-L^{+2}		363	H^2-L^{+0}	325	H^7-L^0 H^0-L^{+5}
							322	H^3-L^0 H^2-L^0 H^4-L^0
	376	387	H^1-L^{+1}	319, 337	380	H^1-L^{+1}	354	H^0-L^{+3} , H^1-L^{+3}
							373	H^2-L^0 H^1-L^{+2} H^0-L^0
		395	H^1-L^0		387	H^1-L^{+0}	386	H^1-L^{+2} H^0-L^{+2} H^1-L^{+1}
		446	H^5-L^{+1} , $H^{11}-L^{+2}$	364 384	434	H^5-L^{+2} $H^{11}-L^{+2}$ H^9-L^{+2}	381	H^0-L^{+1} H^0-L^{+2} H^1-L^{+2}
437	424	465	H^0-L^{+1}		457	H^0-L^{+1} H^0-L^{+2}	411	H^1-L^{+1} , H^1-L^{+0} , H^0-L^{+1}
	485	478	H^0-L^0 H^2-L^{+2}	490	469	H^0-L^0 , H^2-L^{+2}	456	H^0-L^0 , H^0-L^{+1}

		490	H^3-L^{+2} H^7-L^{+2} H^1-L^{+2}		465	H^3-L^{+2} H^7-L^{+2} H^1-L^{+2} H^0-L^{+1}	540	H^0-L^0 H^0-L^{+1} H^0-L^0 H^0-L^{+1} H^1-L^0
590	559	H^2-L^{+2} H^0-L^0	556	532	H^2-L^{+2} H^0-L^0	594	H^2-L^{+2}	

The experimentally obtained pore diameter of MCM-41 is $\sim 68\text{\AA}$, which is much larger compared to that of the zeolite supercage (pore size $\sim 12.5\text{\AA}$). The end-to-end distance of the complex is $\sim 14.3\text{\AA}$. Thus even if the molecule aligns such that the full length is along the diameter of the pore, then the closest non bonded distances of the salen molecule and the wall of the pore is more than 2.5\AA , thus only negligible confinement is offered by the pores. So it is expected that the singlet salen molecule would prevail in such a pore.

3A.2.6. UV-Visible Spectroscopy

For the better understanding of co-ordination environment and geometries of neat and encapsulated complexes, detailed UV-Vis spectroscopic studies are carried out in solution and solid state. For the solution UV-Vis study, chloroform has been selected as suitable solvent among others because it has been well established that Ni(II) salen complex shows distortion in solution with solvents of different dielectric constants like acetic acid, dichloromethane, methanol, chloroform etc. The minimum distortion is observed in chloroform.⁴⁴ Comparative studies of electronic spectra of the 'neat' complex and that of the corresponding ligand reveal the presence of two additional bands at 361 and 437 nm of the complex²⁵ which are assigned as charge transfer transitions. (Experimental and DFT simulated UV-Vis data and spectra of the ligand are given in Figure 3A.9) The solid state (Figure 3A.10, Table 3A.4) electronic transitions of the neat complex appearing at 240 nm is assigned as $\pi-\pi^*$ transition and 332 nm as $n-\pi^*$ transition. The strong evidence of free state complex formation is the appearance of charge transfer (CT) and d-d transitions bands, which are clearly observed in solid state electronic spectrum at 374, 424 and 590 nm respectively. Encapsulated Schiff base complex in zeolite shows $\pi-\pi^*$ transition at 244 nm and $n-\pi^*$ transitions at 288, 319, 337 nm. Charge transfer and d-d bands are appearing at 364, 384, 490

and 556 nm respectively. DFT simulated UV-Vis data supports above observations that these lower energy transitions which are assigned as CT and d-d bands have maximum contribution from metal center of the Schiff base complex.

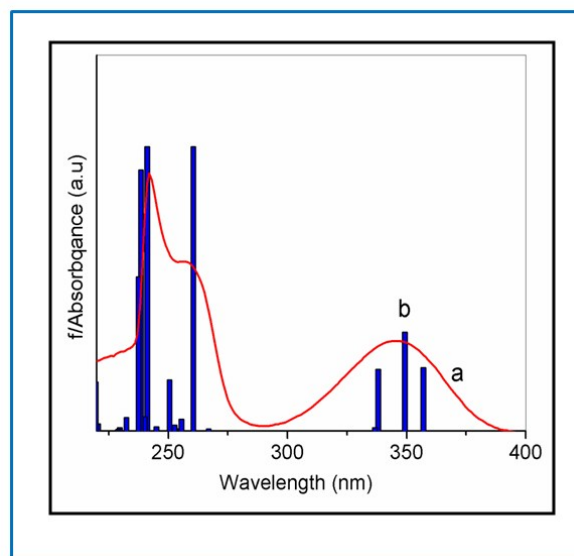


Figure 3A. 9: UV-Vis spectra of (a) L3 in chloroform (b) TD- DFT simulated UV-Vis spectra of L3.

Some interesting observed features are associated with the d-d transition which is broader, more intense⁴⁰ and blue shifted in case of encapsulated complex with the comparison to that of the free state complex, which in turn provides evidence about the reshuffling in electronic energy levels probably because of the distorted geometry of the complex due to steric and electronic constraints imposed by host framework. Experimental spectrum of the encapsulated complex has a very similar nature of d-d transitions with that of the triplet state simulated spectrum where the bands are broader, more intense and blue shifted in comparison to that of diamagnetic neat singlet state encapsulated complex (Figure 3A.10). This observation suggests that encapsulated guest complex has a different geometry around the metal center compared to that in its free state, and the geometry of guest complex is distorted and is probably present in paramagnetic triplet state. A comparative UV-Vis study of encapsulated complex in MCM-41 and Zeolite Y has been done in solid state. The encapsulated NiL3 complex in MCM-41 shows quite similar electronic behavior to that of the free state complex in chloroform rather than that of the complex encapsulated in zeolite Y. (Figure 3A.10) The observation signifies the electronic environment of NiL3-MCM-41 is

much closer to free state complex than encapsulated complex in zeolite Y. Although d-d bands are not very much clearly distinguishable of encapsulated complex in Al-MCM-41, but it is observed that the intensity of d-d region are not much increased and blue shifted as in case of encapsulated complex in zeolite Y. Such type intermediate electronic behavior from free and encapsulated state zeolite Y, of encapsulated complex in Al-MCM-41 can be explained in terms of less steric constrain imposed by the MCM-41 framework due to its large cavity (20 -100 Å) than zeolite Y (12.5Å).

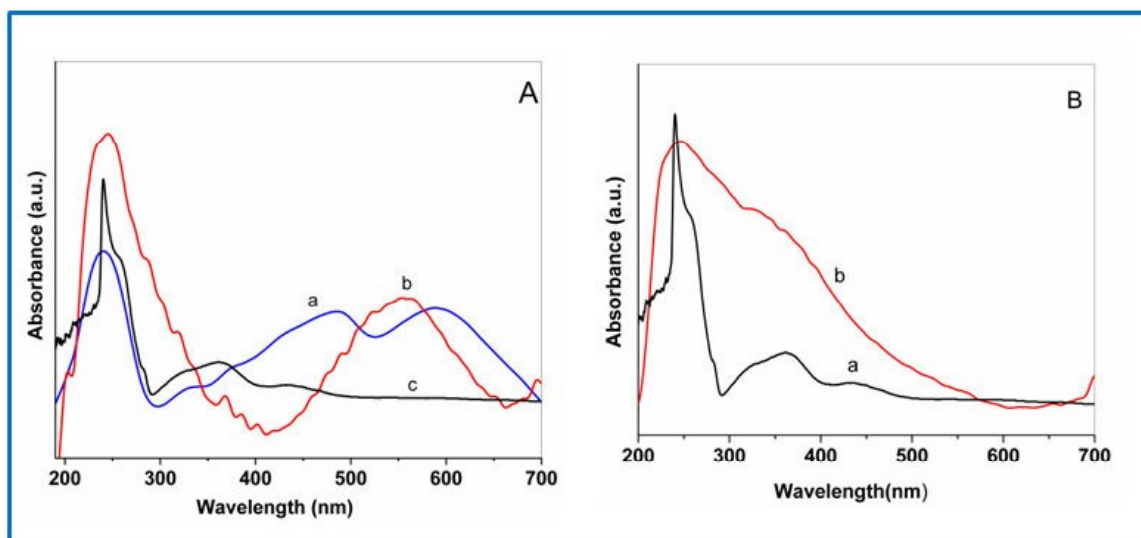


Figure 3A.10: (A) The solid state UV-Vis spectra of (a) NiL3 (b) encapsulated NiL3 in zeolite, (c) NiL3 in chloroform (B) UV-Visible spectra of (a) “neat” NiL3 in chloroform (b) encapsulated NiL3 in complex in MCM-41.

Table 3A.4: UV-Vis data of the “neat” and encapsulated NiL3 in zeolite Y in solid state.

Complex	$\pi-\pi^*$ transitions	$n-\pi^*$ transitions	Charge transfer transitions	d-d transitions
NiL3	240	332, 376	424, 485,	590
NiL3 - Y	244	288,319, 337	364, 384, 490	556

3A.2.7. Magnetic Study

Both the electronic spectroscopic studies and theoretical studies indicate an alteration of the planar geometry of the guest complex when encapsulated in the zeolite-Y, mostly due to the space constraint induced by zeolite. On the other hand, the same studies on the complex encapsulated in the much larger pores of MCM-41, demonstrate significantly less distorted structure compared to that in zeolite. The unstrained neat Ni(II) salen and their derivatives are diamagnetic⁴⁵⁻⁴⁷ with marginal distortion of the NiN₂O₂ plane,⁴⁶ and expectedly the magnetic moments reported for these Ni(II) complexes turn out to be quite close to zero (ranging from 0.39 to 0.54 μ_B), which essentially indicate presence of nearly planar NiN₂O₂ moiety in them. To comprehend the effect of encapsulation particularly on the geometry around the metal ion, magnetic measurements are carried out. The χ vs. T data have been fitted using the Curie-Weiss function along with a temperature independent paramagnetic component (χ_0) arising from Pauli and Van Vleck contributions. Figure 3A.11 shows the temperature variation of inverse of the molar Curie-Weiss susceptibility ($\chi-\chi_0$) for the NiL3 complex encapsulated in zeolite (black open circles). The linear behavior of the curve confirms paramagnetic nature for this complex, which must be arising solely from the metal complex, since the host is diamagnetic.^{33, 48} The moment calculated from the Curie constant for the zeolite encapsulated NiL3 comes out to be 2.33 μ_B and is very close to the moment obtained theoretically. From the theoretical studies a clear indication of lowering of the energy gap between the triplet and singlet states of the complex due to confinement of the complex inside zeolite is observed and the triplet state appears with the magnetic moment of 2.35 μ_B with the spin density on the Ni atom as 1.54. This large value of the moment from the Ni atom reveals that the encapsulation has indeed caused significant change in the NiN₂O₂ plane (Figure 3A.4) by shifting the Ni ion away from it and thereby making the higher lying excited triplet state much more accessible. As a result, considerable fraction of the complex molecules occupy the slightly higher lying excited triplet states (Section 3A.3.6.), which in turn gives rise to a higher moment of the complex. To have a better understanding about the origin of higher magnetic moment of the zeolite encapsulated complex, the magnetic studies of the complex encapsulated in larger pores of MCM-41 are also carried out. Curve (b) of Figure 3A.11 shows the temperature variation of inverse Curie-Weiss molar susceptibility ($\chi-\chi_0$) for the NiL3 complex encapsulated in MCM. However, the nonlinearity of this

susceptibility curve indicates presence of other weaker magnetic contributions in this sample, visible only at higher temperature i.e. when the paramagnetic contribution is reduced.

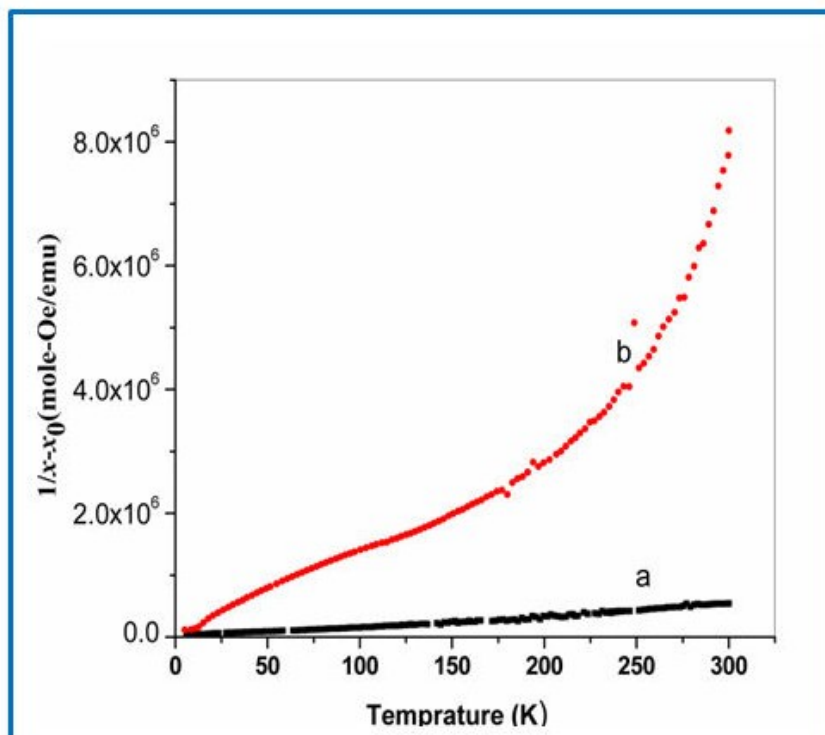


Figure 3A.11: The $1/\chi - \chi_0$ Vs T graph of (a) NiL3 complex in zeolite Y and (b) NiL3 complex in MCM-41.

Fitting of the dominant low temperature paramagnetic contribution indicates a low magnetic moment of $0.53 \mu_B$ in this sample. This value of the moment is exactly in agreement with the moment available in the literature⁴² for such kind of systems in their neat forms, which essentially proves that the large pores of MCM are able to accommodate the complex without any further distortion. Therefore, the geometry adopted by the metal complex is expected to be the one observed in the free state.

3A.3. CONCLUSIONS

This section presents comparative spectroscopic and magnetic studies of the NiL3 complex encapsulated in hosts of different pore sizes like zeolite-Y, MCM-41 and in the unencapsulated free state. The focus is on the effect of the size and topology of the pores of the host on the geometry adopted by the planar complex on encapsulation. Powder X-ray

diffraction and vibrational spectroscopic studies support the successful encapsulation of the NiL3 inside the supercage of zeolite-Y and in the pores of MCM-41 where keeping the host frameworks intact. Electronic spectrum of the zeolite-Y encapsulated NiL3 complex shows that charge transfer and *d-d* bands are mainly intensified and blue shifted whereas the spectrum of the complex in MCM-41 resembles quite closely to the solution spectrum taken in chloroform. The absorption bands affected by encapsulation inside zeolite are the transitions associated with the metal center which provides a hint of the metal being shifted from the NiN₂O₂ plane. From the theoretical studies it is observed that the planar neat complex undergoes a distortion to fit into the supercage and the experimentally observed electronic spectrum of encapsulated complex has much closer resemblance with the one simulated for distorted triplet state complex compared to the one for distorted singlet state. These observations clearly indicate that due to the larger pore size in compared to the size (end-to-end distance) of the complex, MCM-41 does not impose the steric constraints on the encapsulated complex whereas zeolite with a smaller pore size does. The electronic spectra indicate that encapsulation inside zeolite supercage forces the complex to take up a distorted geometry which in turn, makes the energetically higher lying triplet state more accessible. Theoretical studies indeed show the stabilization of encapsulated triplet state compared to the free isolated singlet ground state.

The observed electronic spectrum of the encapsulated complex resembles quite closely the calculated optical spectrum of the complex in triplet state rather than the singlet state. The theoretical magnetic moment calculated for the complex inside the zeolite supercage shows a magnetic moment of 2.35 μ_B with spin density on Ni as 1.54 when the complex is in the triplet state. The experimental magnetic studies detect the zeolite encapsulated complex as clearly paramagnetic with the magnetic moment of 2.33 μ_B . All these experimental and theoretical observations definitely prove that topology of the zeolite supercage has a pronounced effect on the structure of the complex. To fit into the cavity, the complex has undergone a distortion (shown in Figure 3A.4 c), which drives away the Ni atom out of the plane of NiN₂O₂ moiety. This distortion lowers the energy gap between the triplet and singlet states and causes a dramatic change of the magnetic property of the complex from diamagnetic to paramagnetic, which is also reflected in the reduced energy gap between the encapsulated singlet and triplet states. This enhancement of the magnetic moment is clearly

related to the extent of distortion of the NiL3 from planar geometry since when the larger voids of mesoporous MCM-41 encapsulates the complex, it can be accommodated without significant loss of planarity. Encapsulation in MCM-41 allows the complex to retain its free state geometry by leaving the complex largely diamagnetic as expected in its free state. The planar diamagnetic NiL3 complex becomes significantly paramagnetic when it is encapsulated in a host with pores of dimension comparable with the end-to-end distance of the complex.

REFERENCES

1. K. J. Balkus and A. G. Gabrielov, *J. Inclusion Phenom. Mol. Recognit. Chem.*, 1995, **21**, 159-184.
2. C. R. Jacob, S. P. Varkey and P. Ratnasamy, *Appl. Catal., A*, 1999, **182**, 91-96.
3. P. K. Dutta, *J. Inclusion Phenom. Mol. Recognit. Chem.*, 1995, **21**, 215-237.
4. D. E. De Vos, P. P. Knops-Gerrits, R. F. Parton, B. M. Weckhuysen, P. A. Jacobs and R. A. Schoonheydt, *J. Inclusion Phenom. Mol. Recognit. Chem.*, 1995, **21**, 185-213.
5. M. L. Cano, A. Corma, V. Fornés, H. García, M. A. Miranda, C. Baerlocher and C. Lengauer, *J. Am. Chem. Soc.*, 1996, **118**, 11006-11013.
6. M. Álvaro, J. F. Cabeza, A. Corma, H. García and E. Peris, *J. Am. Chem. Soc.*, 2007, **129**, 8074-8075.
7. C. K. Modi, P. M. Trivedi, S. K. Gupta and P. K. Jha, *J. Incl. Phenom. Macrocycl. Chem.*, 2012, **74**, 117-127.
8. G. A. Ozin and C. Gil, *Chem. Rev.*, 1989, **89**, 1749-1764.
9. K. Kervinen, P. C. A. Bruijninx, A. M. Beale, J. G. Mesu, G. van Koten, R. J. M. Klein Gebbink and B. M. Weckhuysen, *J. Am. Chem. Soc.*, 2006, **128**, 3208-3217.
10. A. Corma and H. Garcia, *Eur. J. Inorg. Chem.*, 2004, **2004**, 1143-1164.
11. N. HERRON, *ChemInform*, 1987, **18**.

12. C. R. Jacob, S. P. Varkey and P. Ratnasamy, *Microporous Mesoporous Mater.*, 1998, **22**, 465-474.
13. D. Srinivas and S. Sivasanker, *Catal. Surv. Asia*, 2003, **7**, 121-132.
14. F. Bedioui, E. De Boysson, J. Devynck and K. J. Balkus, *J. Chem. Soc., Faraday Trans.*, 1991, **87**, 3831-3834.
15. R. F. Parton, L. Uytterhoeven and P. A. Jacobs, in *Studies in Surface Science and Catalysis*, eds. J. B. C. B. D. D. G. P. R. M. M. Guisnet and C. Montassier, Elsevier, 1991, vol. Volume 59, pp. 395-403.
16. K. K. Bania and R. C. Deka, *J. Phys. Chem. C*, 2011, **115**, 9601-9607.
17. K. Mizuno and J. H. Lunsford, *Inorg. Chem.*, 1983, **22**, 3484-3486.
18. B. M. Weckhuysen, A. A. Verberckmoes, I. P. Vannijvel, J. A. Pelgrims, P. L. Buskens, P. A. Jacobs and R. A. Schoonheydt, *Angew. Chem. Int. Ed.*, 1996, **34**, 2652-2654.
19. M. J. Sabater, A. Corma, A. Domenech, V. Fornes and H. Garcia, *Chem. Commun.*, 1997, DOI: 10.1039/A701337J, 1285-1286.
20. C. Jin, W. Fan, Y. Jia, B. Fan, J. Ma and R. Li, *J. Mol. Catal. A: Chem.*, 2006, **249**, 23-30.
21. J. Poltowicz, K. Pamin, E. Tabor, J. Haber, A. Adamski and Z. Sojka, *Appl. Catal., A*, 2006, **299**, 235-242.
22. M. Silva, C. Freire, B. de Castro and J. L. Figueiredo, *J. Mol. Catal. A: Chem.*, 2006, **258**, 327-333.
23. M. R. Maurya, S. J. J. Titinchi, S. Chand and I. M. Mishra, *J. Mol. Catal. A: Chem.*, 2002, **180**, 201-209.
24. S. Deshpande, D. Srinivas and P. Ratnasamy, *J. Catal.*, 1999, **188**, 261-269.

25. K. K. Bania, D. Bharali, B. Viswanathan and R. C. Deka, *Inorg. Chem.*, 2012, **51**, 1657-1674.
26. K. K. Bania, G. V. Karunakar, K. Goutham and R. C. Deka, *Inorg. Chem.*, 2013, **52**, 8017-8029.
27. R. F. Parton, I. F. J. Vankelecom, M. J. A. Casselman, C. P. Bezoukhanova, J. B. Uytterhoeven and P. A. Jacobs, *Nature*, 1994, **370**, 541-544.
28. S. K. Tiwary and S. Vasudevan, *Inorg. Chem.*, 1998, **37**, 5239-5246.
29. Y. Umemura, Y. Minai and T. Tominaga, *J. Phys. Chem. B*, 1999, **103**, 647-652.
30. S. Ray and S. Vasudevan, *Inorg. Chem.*, 2003, **42**, 1711-1719.
31. M. Jafarian, M. Rashvand avei, M. Khakali, F. Gobal, S. Rayati and M. G. Mahjani, *J. Phys. Chem. C*, 2012, **116**, 18518-18532.
32. W. H. Quayle, G. Peeters, G. L. De Roy, E. F. Vansant and J. H. Lunsford, *Inorg. Chem.*, 1982, **21**, 2226-2231.
33. W. H. Quayle and J. H. Lunsford, *Inorg. Chem.*, 1982, **21**, 97-103.
34. V. B. Fenelonov, A. Y. Derevyankin, S. D. Kirik, L. A. Solovyov, A. N. Shmakov, J. L. Bonardet, A. Gedeon and V. N. Romannikov, *Microporous Mesoporous Mater.*, 2001, **44-45**, 33-40.
35. X. S. Zhao, G. Q. Lu and G. J. Millar, *Ind. Eng. Chem. Res.*, 1996, **35**, 2075-2090.
36. R. Nares, J. Ramírez, A. Gutiérrez-Alejandre and R. Cuevas, *Ind. Eng. Chem. Res.*, 2009, **48**, 1154-1162.
37. B. Dutta, S. Jana, R. Bera, P. K. Saha and S. Koner, *Appl. Catal., A*, 2007, **318**, 89-94.
38. R. M. Barrer, *Hydrothermal chemistry of zeolites*, Academic Press, 1982.
39. M. Asadi, K. A. Jamshid and A. H. Kyanfar, *Inorg. Chim. Acta*, 2007, **360**, 1725-1730.

40. R. Ganesan and B. Viswanathan, *J. Phys. Chem. B*, 2004, **108**, 7102-7114.
41. H. Yoon, T. R. Wagler, K. J. O'Connor and C. J. Burrows, *J. Am. Chem. Soc.*, 1990, **112**, 4568-4570.
42. J. E. Reed, A. A. Arnal, S. Neidle and R. Vilar, *J. Am. Chem. Soc.*, 2006, **128**, 5992-5993.
43. A. Arola-Arnal, J. Benet-Buchholz, S. Neidle and R. Vilar, *Inorg. Chem.*, 2008, **47**, 11910-11919.
44. M. A. Siegler and M. Lutz, *Cryst. Growth Des.*, 2009, **9**, 1194-1200.
45. H.-C. Zhang, W.-S. Huang and L. Pu, *J. Org. Chem.*, 2001, **66**, 481-487.
46. A. Boettcher, H. Elias, E. G. Jaeger, H. Langfelderova, M. Mazur, L. Mueller, H. Paulus, P. Pelikan, M. Rudolph and M. Valko, *Inorg. Chem.*, 1993, **32**, 4131-4138.
47. H. Yoon and C. J. Burrows, *J. Am. Chem. Soc.*, 1988, **110**, 4087-4089.
48. D. N. Stamires and J. Turkevich, *J. Am. Chem. Soc.*, 1964, **86**, 749-757.



Chapter 3: Part B

**Nickel Schiff-Base Complexes in Zeolite Y: A
Correlation with the Adopted Geometry with
Magnetization and Catalytic Activity**

3B.1. INTRODUCTION

Zeolite embedded metal complexes are potential catalysts for various catalytic processes,¹ as the complexes have modified reactivities and selectivities from their solution states.^{2, 3} Furthermore, the zeolites are thermally stable with different active sites and act as eco-friendly medium for different processes. They are also known as 'solid acid' due to the presence of Brønsted and Lewis acid sites and even can be used like sulphuric acid in the chemical reactions.^{4,6} Many frequent reports in the literature have depicted enhanced reactivity of these systems as catalysts with additional benefits like easy separation, reusability and resistivity at higher temperature.^{7, 8, 9} The encapsulated transition metal complexes like phthalocyanine, bipyridyl and Schiff base ligands in zeolites are popularly called as 'zeozymes' and well recognized as bio mimetic systems or¹⁰ since they show the structural and functional analogy with biological enzymes.^{11, 12} These heterogeneous resembling 'ship-in-a-bottle' systems offer a novel route to couple the reactivity of metal complex with special structural robustness of zeolites. It is quite exciting that the guest complex with comparable or slightly larger molecular dimension in comparison to dimension of the zeolite-Y supercage, experiences steric restrictions imposed by the rigid walls of host framework and adopts an altered geometry to accommodate itself inside the host cavity.^{13, 14} Such induced structural changes might be associated with the tailored reactivity. Therefore, it is very important to study the influence of the architecture and topology of the host framework on the geometry of guest complex so that the adapted reactivity is better understood. The modified catalytic activity and selectivity of the encapsulated complexes originates from host–guest interaction in the hybrid system. Rudy F. Patron et al reported that iron phthalocyanine complex in zeolites Y is a mimic of cytochrome P-450 and 10 times more efficient for oxidation of C-H bond in mono branched hydrocarbons.¹² The authors have reported that zeolite framework exercises the steric constraint on active site of FePc complex as does the protein mantle in cytochrome P-450. In another report P.A. Jacob et.al have reported that the manganese complexes in zeolites X and Y are selective towards alkenes oxidation reactions.¹⁵ The zeolite encapsulated metal Schiff-base complexes are well explored as catalysts for the various reactions like oxidation of toluene, benzyl alcohol, cyclohexane, ethyl benzene methyl phenyl sulphide, and styrene,^{2, 3, 5, 7, 16-19} with mild oxidants like H₂O₂ and TBHP. A recent report has also explored the other dimensions of

these systems and found that the amine functionalized ionic liquid encapsulated in zeolites Y shows capability for CO₂ capture.²⁰

Catalysis of zeolite encapsulated complexes is well investigated research area however the impact of encapsulation on the structural alteration of the guest complex still remains relatively less studied, though the enhanced selectivity and modified reactivity might have strong correlation with altered geometry adopted by the encapsulated complex. There are only few reports available in the literature,^{13, 14, 21, 22} which have illustrated the influence of the topology of the void on the geometry of encapsulated complex and its consequences in terms of change in electronic, physical, catalytic and redox properties of encapsulated system. Here, we report the interesting electronic, magnetic and catalytic behavior and correlation between adopted geometry and functionality of the nickel complexes of Schiff-base ligands with general formula: *N,N*-bis(salicylidene)ethylenediamine (L1), *N,N*-bis(5-bromo-salicylidene)ethylenediamine (L4) and *N,N*-bis(5-methoxy-salicylidene)ethylenediamine (L6) abbreviated as NiL1, NiL4 and NiL6 respectively (Given in Figure 3B.1). These complexes follow an increasing order in terms of their molecular dimensions, which are 12.94 Å, 14.72 Å and 15.09 Å for NiL1, NiL4 and NiL6 respectively.

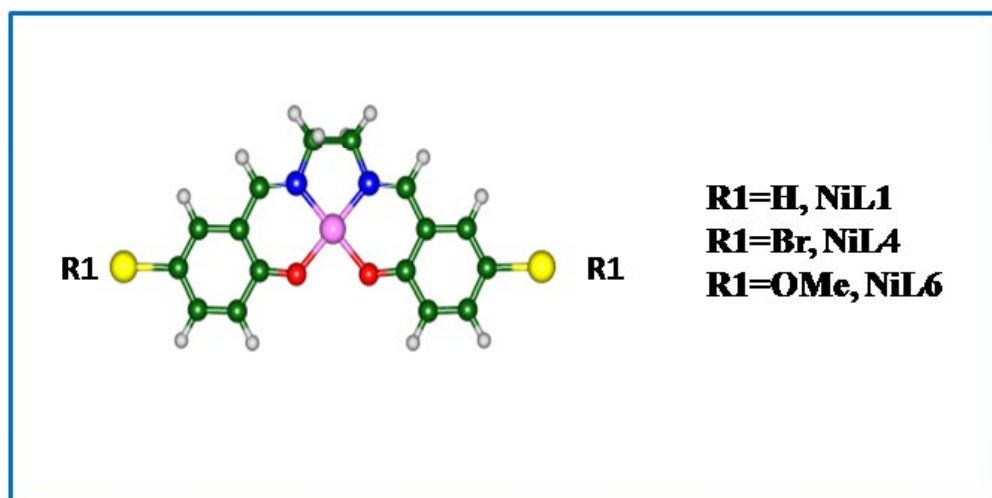


Figure 3B.1: Schematic structure for the Ni-salen complexes in free state.

3B.2. RESULTS AND DISCUSSION

Synthesis of ligands, complexes in free as well as encapsulated states is already discussed in chapter 2 under experimental sections 2.2.1-2.2.6.

3B.2.1. Elemental Analysis

The pure Na-zeolite Y has the unit cell formula as $\text{Na}_{58}\text{Al}_{58}\text{Si}_{136}\text{O}_{388}\cdot y\text{H}_2\text{O}$ and Si/Al ratio is 2.34. The elemental analysis (EDS spectra) of encapsulated complexes NiL1-Y, NiL4-Y and NiL6-Y have suggested that Si/Al ratio remains unaffected even after the encapsulation for all the cases [Appendix A4, A6 and A7] indicating that the dealumination doesn't take place during the process of encapsulation. The concentration of nickel ion in the Ni-exchanged zeolite Y is 0.92 wt% which is greater than that of the all encapsulated complexes. The concentrations of nickel are 0.59 wt%, 0.47 wt% and 0.52 wt% for NiL1-Y, NiL4-Y and NiL6-Y respectively. During the process of encapsulation of the complex inside the supercage of zeolite, slight leaching of metal ion is expected which ultimately leads to the reduction of the wt% of nickel in encapsulated metal complexes.

3B.2.2. XRD Analysis

The zeolite Y encapsulated nickel salen complexes are synthesized via flexible ligand synthesis method²² in the cavity, keeping the host framework integrity preserved, unreacted ligands and surface adsorbed complexes are removed by Soxhlet extraction using sequence of different solvents. The XRD patterns of pure zeolite Y, Ni-zeolite Y, NiL1-Y, NiL4-Y and NiL6-Y complexes essentially signify the crystalline nature of all the materials (given in Figure 3B.2). Comparison of the XRD diffractograms of NiL1-Y, NiL4-Y and NiL6-Y samples and that of the pure zeolite Y, demonstrate no shift in peak positions when compared. This observation is indeed a significant one as it implies the integrity of host framework preserved even after the encapsulation of a large complex into it. However, XRD patterns of NiL1-Y, NiL4-Y and NiL6-Y evidently illustrate a considerable intensity reversal ($I_{220} < I_{311}$) of the peaks at $2\theta = 10^\circ$ and 12° in comparison to that in the XRD patterns of pure and Ni exchanged zeolite Y. This observation empirically correlates with the fact that a large complex is certainly present inside the zeolite Y cavities.^{23, 24} The absence of new peaks in XRD patterns of encapsulated complexes is a signature of formation of the complexes in low concentrations inside the host lattice.

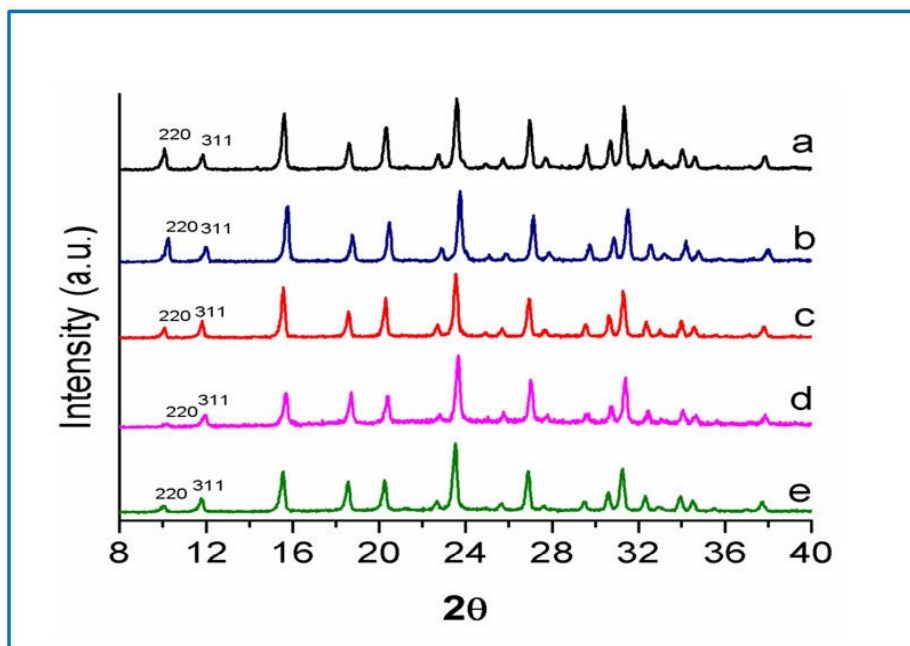


Figure 3B.2: XRD patterns of (a) pure zeolite Y, (b) Ni-exchanged Y, (c) NiL1-Y, (d) NiL4-Y and (e) NiL6-Y complexes.

3B.2.3. Scanning Electron Microscopy

SEM-EDS study of pure zeolite Y, NiL1-Y, NiL4-Y and NiL6-Y are carried out. (Shown in Figure 3B.3) In the SEM images of zeolite with entrapped complexes, zeolitic boundaries are evidently visible and comparable with that of the pure zeolite Y. This is mainly due to absence of unreacted species or impurities on the surface of host lattice.^{25, 26}

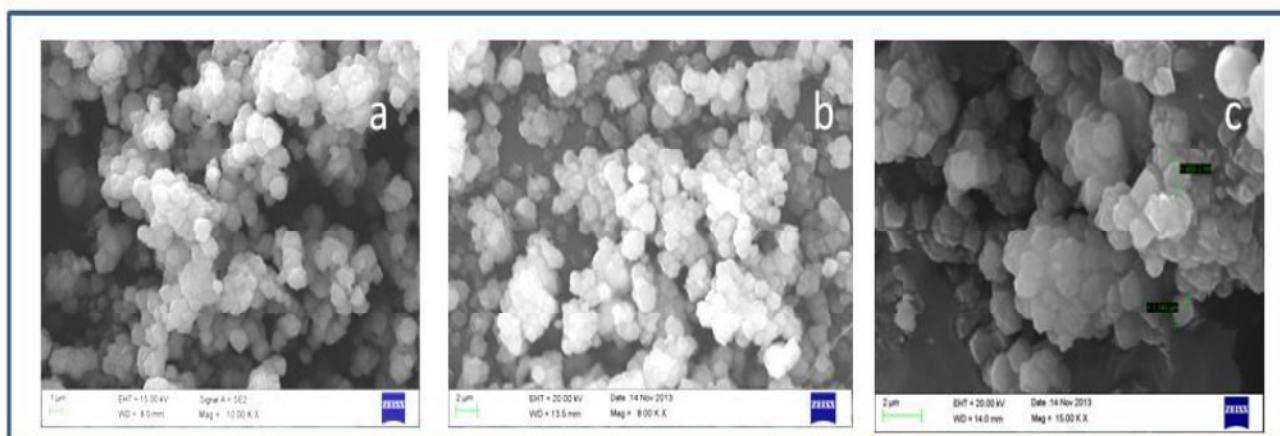


Figure 3B.3: SEM images of pure (a) zeolite Y, and (b) NiL1-Y, (c) NiL6-Y after Soxhlet extraction.

3B.2.4. X-ray Photoelectron Spectroscopy (XPS)

The presence of metal complex in the zeolite lattice has been confirmed by the X-ray photoelectron spectroscopy (The XPS survey spectra of the free state complex (NiL1) and encapsulated complexes (NiL1-Y, and NiL6-Y) are shown in the Figure 3B.4.-3B.6. It reveals the presence of C, N, O, Na, Si, Al, Ni(II) in their respective chemical states in the complexes as expected from the literature.²⁷⁻³¹ The low XPS peak intensities observed for nickel in the NiL1-Y, and NiL6-Y complexes are perfectly in agreement with the observations of other concentration dependent studies like EDX, IR and UV-Visible spectroscopy, which clearly indicates that the concentrations of nickel is quite low in case of encapsulated metal complex. The presence of Ni(II) metal in the free state complex is confirmed by the existence of $2p_{3/2}$ and $2p_{1/2}$ peaks in the XPS spectra at the binding energies 855.27 and 872.47 eV respectively.²⁷ The existence of these two peaks suggests the nickel metal is indeed present in the +2 oxidation state, furthermore the absence of any shake up and satellite peak behind 878 eV confirms that the complex actually exists in the square planar geometry not in the octahedral geometry.^{27, 30} The carbon (1s) XPS spectra (Data given in Table 3B.1) are intense and broad for the both state complexes, which is further deconvoluted into two peaks. XPS binding energy data have suggested the the presence of two different types of carbon atoms in the complexes both in the neat and encapsulated states, which are identified as sp^3 and sp^2 carbon atoms. Similarly, the nitrogen (1s) XPS traces are further deconvoluted into two peaks at binding energies which are attributed to (M-N) and (N=C) correspondingly. Oxygen (1s) XPS peaks with shoulder peak are mainly due to (C-O) and (M-O) respectively. NiL1-Y and NiL6-Y show the same pattern of XPS spectra with the negligible shifts in peak positions, along with the Si (2p), Al (2p) and Na (1s) XPS signals, which confirm the occurrence of the nickel – Schiff-base complex in the zeolite Y. The $2p_{3/2}$ and $2p_{1/2}$ peaks of Ni (II) appear slightly shifted from those of the free state complex which eventually signifies the slight change in the coordination geometry of the encapsulated complex. Carbon (1s) deconvoluted spectra of encapsulated complexes also suggest the presence of sp^3 and sp^2 types of carbon atoms and XPS spectra of nitrogen (1s) corresponding to (M-N, N=C) and oxygen (1s) corresponding (M-O, C-O) also in accordance with those of its neat state, (Binding energy data are given in Table 3B.1) Nickel $2p_{3/2}$ and $2p_{1/2}$ XPS peaks of NiL6-Y is not very clear, however the appearance of C(1s), N(1s), O(1s), Na(1s), Si(2p), Al(2p) XPS

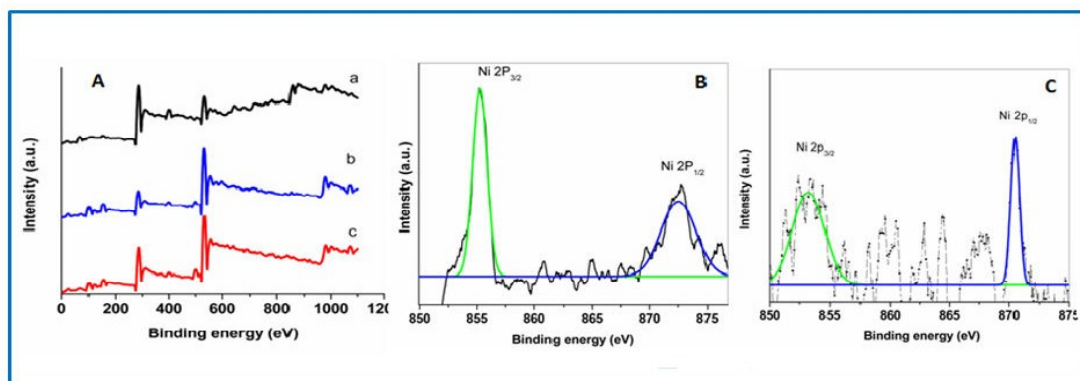


Figure 3B.4: (A) XPS survey spectra (a) NiL1, (b) NiL1-Y, and (c) NiL6-Y, and high resolution XPS spectra of Ni (2p) for (B) NiL1 and (C) NiL1-Y. (Black colored graphs are experimental data and green and blue colored peaks are peak fitted data)

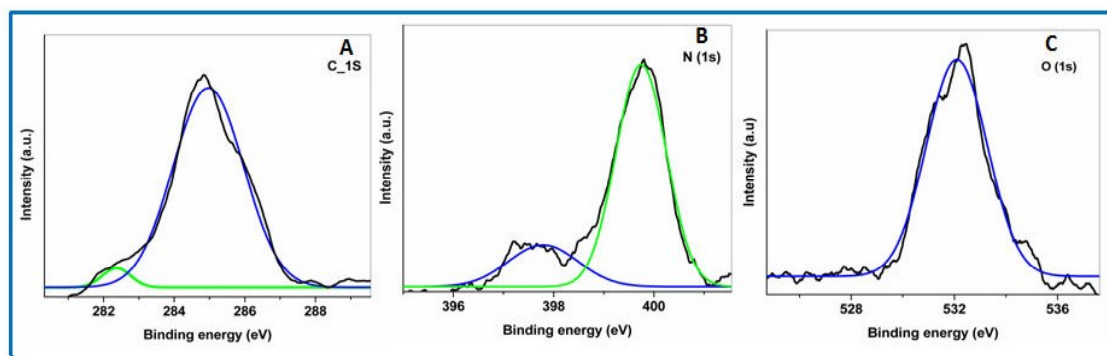


Figure 3B.5: High resolution XPS spectra of (A) C (1s), (B) N (1s) and (C) O (1s) for NiL1. (Black colored graphs are experimental data and green and blue colored peaks are peak fitted data)

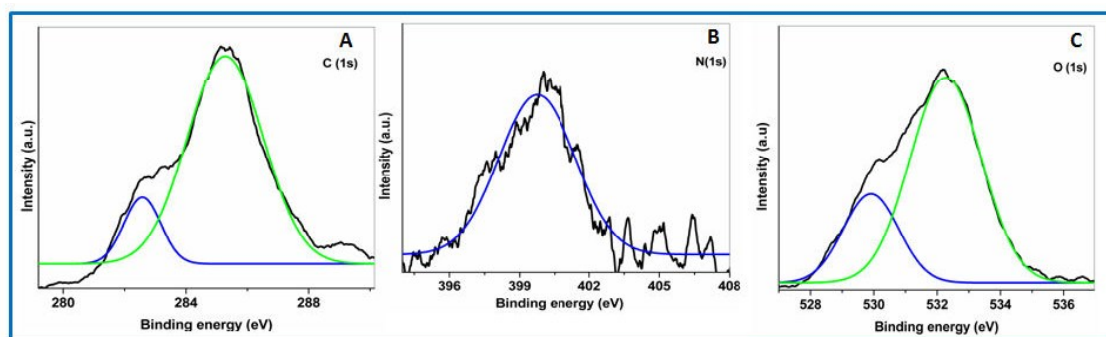


Figure 3B.6: High resolution XPS spectra of A) C (1s), (B) N (1s) and (C) O (1s) for NiL1-Y. (Black colored graphs are experimental data and green and blue colored peaks are peak fitted data)

peaks for NiL6-Y complex are in the agreement with the peaks observed for NiL1 and NiL6-Y complexes, which clearly indicates the complex formation has taken place during encapsulation process in zeolite Y.

Table 3B.1: Binding energy of the neat and encapsulated complex.

S.No	Samples	Si (2p)	Al (2p)	C (1s)	O (1s)	N(1s)	Ni ²⁺ (2p)	$\Delta 2p$
1.	NiL1	-	-	284.86, 282.7	532.19, 531.36	399.78, 397.77	855.27, 872.47	17.20
2.	NiL1-Y	102.96	75.33	285.27, 282.57	532.24, 529.96	399.70, 397.55	853.25, 870.50	17.25
3.	NiL6-Y	103.71	74.68	286.10, 283.32	533.22, 530.58	400.64	854.63, 872.22	17.59

3B.2.5. IR Spectroscopy

FTIR spectral data of ligands (given in Figure 3B.7 and Table 3B.2), pure zeolite Y and nickel Schiff base complexes in neat as well as encapsulated state have been recorded. IR spectroscopic study has provided information about the integrity of zeolite Y framework and also the successful complex formation inside the host framework. On comparing the IR spectra of the encapsulated complexes with the IR spectra of pure zeolite Y, all characteristic zeolitic peaks for NiL1-Y, NiL4-Y and NiL6-Y systems are found unaffected. The major zeolitic IR bands are observed in the region of (450-1200) cm^{-1} and two peaks appeared at 1643 cm^{-1} and 3500 cm^{-1} region. The IR bands at 560, 717, 786, and 1018 cm^{-1} are assigned as (Si/Al-O)₄ bending mode, double ring, symmetric stretching and asymmetric stretching vibration respectively.³² whereas IR bands at 3500 cm^{-1} and 1643 cm^{-1} are originated due to the surface hydroxylic group and lattice water molecules respectively.²⁵ The presence of these bands without any shift or alternation in the IR spectra of NiL1-Y, NiL4-Y and NiL6-Y complexes actually have shown retention of the structure of host lattice. IR peaks of the encapsulated complexes are mostly obscure, because of the presence of the strong zeolitic bands in the (450– 3500) cm^{-1} region. A few IR peaks of low intensities are observed in the range of (1600-1200) cm^{-1} which are mainly associated with the guest complex and found to be suitable for the investigation of synthesis of the complex inside the supercage, because zeolite in particular doesn't show peaks in this region whereas the Schiff-base complex show its major characteristics bands like C=C, C=N and C-O stretching³³ and C-H deformation.

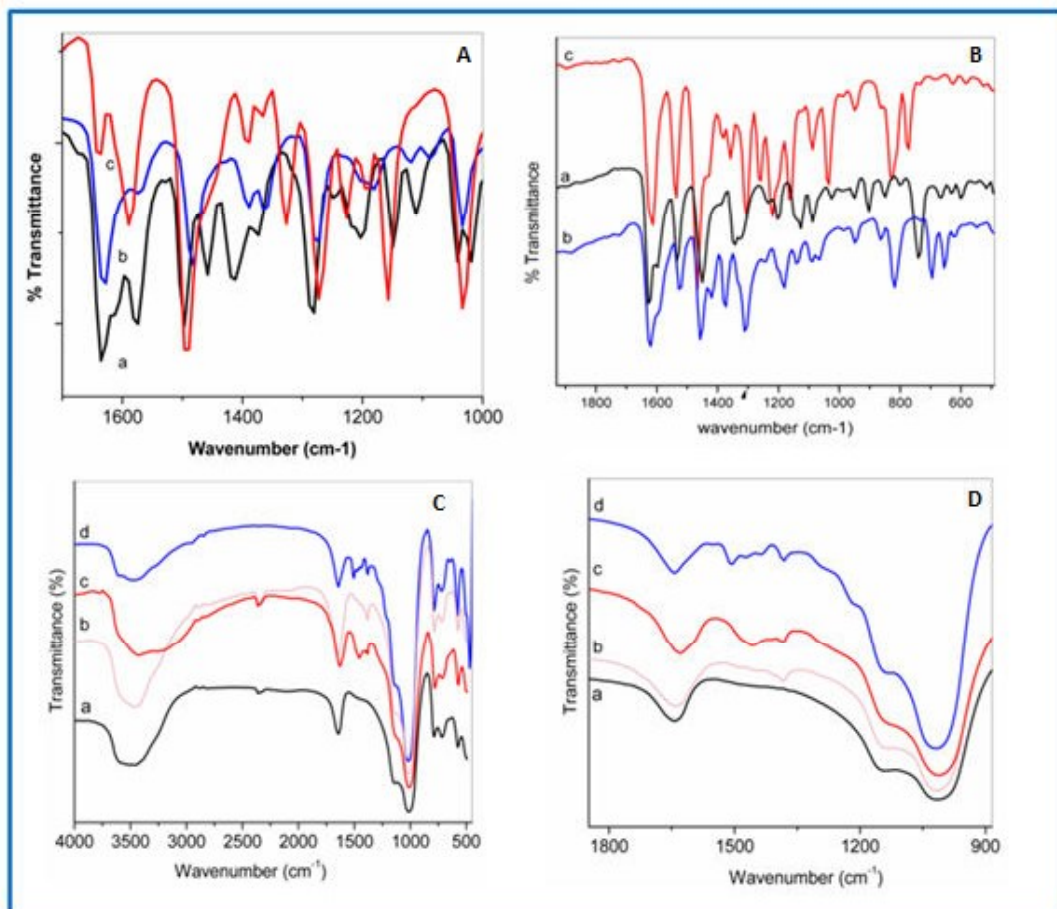


Figure 3B.7: (A) FTIR spectra of Ligands (a) L1, (b) L4 and (c) L6. (B) (A) FTIR spectra of free state complexes (a) NiL1, (b) NiL4 and (c) NiL6. (C) FTIR spectra of (a) pure zeolite Y, (b) NiL1-Y, (c) NiL4-Y and (d) NiL6-Y. (D) Enlarged view FTIR spectra of (a) pure zeolite Y, (b) NiL1-Y, (c) NiL4-Y and (d) NiL6-Y.

Table 3B.2: FTIR spectral data (in cm^{-1}) for the ligands and both state complexes.

Samples	(C=N str.)	(C=C str.)	(C-H def.)	(C-O str.)
L1	1633	1557, 1488, 1451	1374	1286
NiL1	1626	1537, 1451	1347	1234

NiL1-Y	1641	1491, 1449	1381	Merged with zeolite band
L4	1633	1572, 1481	1390	1361
NiL4	1621	1529, 1460	1372,	1307
NiL4-Y	1629	1456	1383	1282
L6	1639	1589, 1494	1325	1272
NiL6	1612	1537, 1468	1306,	1221
NiL6-Y	1642	1509, 1471	1380	1145

3B.2.6. Solid state UV-Visible Study

To explore the environment around the metal in detail, comparative optical have been carried out for free as well as encapsulated state complexes. Solid state UV-Visible electronic spectra of the complexes in free and encapsulated states are recorded (Shown in Figure 3B.8). The intensity of electronic bands of the encapsulated complexes is generally weak due to very low concentration of metal-ion and also due to the presence of guest complexes inside the host cavity. In the electronic spectrum, the high energy transitions are mainly identified as intraligand transitions (π - π^* and n - π^*) and relatively lower energy transitions are recognized as charge transfer and d-d transitions,³⁴ which mainly originate from the metal center of the complexes. It has been observed for each complex that the intraligand transitions remain more or less unshifted (Table 3B.3), but transitions in the range of (550-595) nm, which are instigated from the metal center are primarily affected i.e., intensified⁷ and blue shifted on encapsulation (Discussed in Chapter 3A). Such behavior of the guest complexes clearly indicate the alteration of the geometry of the encapsulated complexes especially around the metal center while encapsulated, sited in the center of planar environment. From TD-DFT simulated electronic spectra, similar pattern of intensification and blue shift in d-d bands are observed in the electronic spectrum of 5-hydroxy nickel salen complex after encapsulation in zeolite Y, Furthermore it has been identified that 5-hydroxy nickel salen complex in encapsulated state, suffers from the distortion of the geometry with the metal center moved

away from N_2O_2 plane (Discussed in Chapter 3A). B. de Castro et.al have reported quite an exciting observation which concludes that the change in the co-ordination sphere by replacing N_2O_2 proximity with N_2OS or N_2S_2 moiety consequently leads to the changes in the optical properties, primarily the d-d transitions.³⁵ Planarity of the co-ordination sphere can also be disturbed by introducing different substituent groups on the phenyl rings of the salen ligand. An electron withdrawing group (-Cl, -Br) enhances the distortion around the metal center of the planar salen complex,^{7, 35} whereas an electron donating group (-OCH₃) favours the planarity around the metal center. Such electronic effects have been adequately studied on the porphyrin metal complexes, authors have reported that electron donating and electron withdrawing groups have introduced the push and pull effect on the complex, and the consequence has been observed on the dipole moment of the complex.³⁶

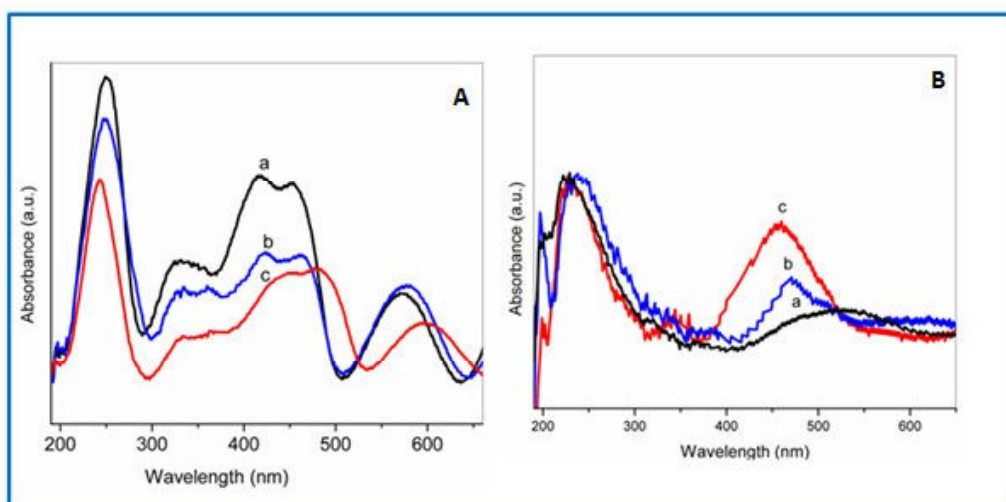


Figure 3B.8: (A). The solid state UV-Vis spectra of “neat” complex (a) NiL1, (b) NiL4 and (c) NiL6. (B) The solid state UV-Vis spectra of encapsulated complexes in zeolite Y, (a) Pure zeolite Y, (b) NiL1-Y, (c) NiL4-Y and (d) NiL6-Y.

A fascinating correlation between molecular dimensions of the encapsulated complexes and extent of blue shift and intensification of d-d bands is observed, the blue shift of the d-d bands generally assigned as $d_z^2 - d_{xy}$ transitions³⁷ has come into notice. Our optical studies reveal that encapsulated NiL6 complex (largest molecular dimension of 15.09 Å) exhibits the maximum intensified and blue shift in d-d transition (84 nm) among all three complexes. This pattern is also followed by encapsulated NiL4 and NiL1 complexes according to their magnitude of molecular dimension, NiL4 shows moderate intensified d-d band and blue

shift is around 68 nm whereas NiL1 shows the comparatively less intensified and lowest shift (35 nm) in d-d transition after encapsulation in the zeolite-Y.

Table 3B.3. Solid state UV-Visible data of complexes in free and encapsulated state.

S.No	Samples	π - π^* transitions	n- π^* transitions	CT transitions	d-d transitions
1.	NiL1	251	323, 355	413,453	570
2.	NiL1-Y	242	320, 360	Not observed	535
3.	NiL4	250	333, 361	420, 466	577
4.	NiL4-Y	249	335, 365	470	509
5.	NiL6	243	329, 363	440, 485	595
6.	NiL6-Y	244	320- 360	459	511

The correspondence between the size and magnitude of the observed blue shift appears rational, because in order to fit into the supercage, the largest NiL6 complex requires to undergo maximum distortion from its planar geometry. Whereas NiL4 complex is moderately large and NiL1 complex is comparable with the diameter of the zeolite supercage, hence distortion in the planar geometry is anticipated from both the NiL4 and NiL6 complexes hence the expected order of the blue shift of the d-d transition can be attributed to the extent of distortion undergone by the complex after encapsulation in zeolite Y

3B.2.7. Magnetic Study

FC measurements by using the SQUID magnetometer have been carried out for all the complexes in their neat and encapsulated states. Although these complexes in their neat states are diamagnetic with magnetic moment near to zero (0.45 – 0.69 BM) essentially demonstrating the planarity of N_2O_2 moiety around the d^8 Ni(II) centre,^{38 39} under encapsulation they have shown specifically different magnetic behavior. The molar susceptibility data of the complexes are presented in Figure 3B.9. Encapsulated complexes

are showing unusual magnetic behavior and enhanced magnetization, definitely originated from the nickel complexes because pure zeolite Y is diamagnetic in nature.²⁴ Such observed fundamentally different magnetic behaviour the guest nickel salen complexes are apparently initiated from the non-planar geometry around the metal of the encapsulated complexes. As a result under non-planar geometry, Ni ion experiences a electronic environment different from that in its free state which in turn imposes alteration in the ordering of molecular energy levels as planarity of NiN₂O₂ moiety is no more maintained.

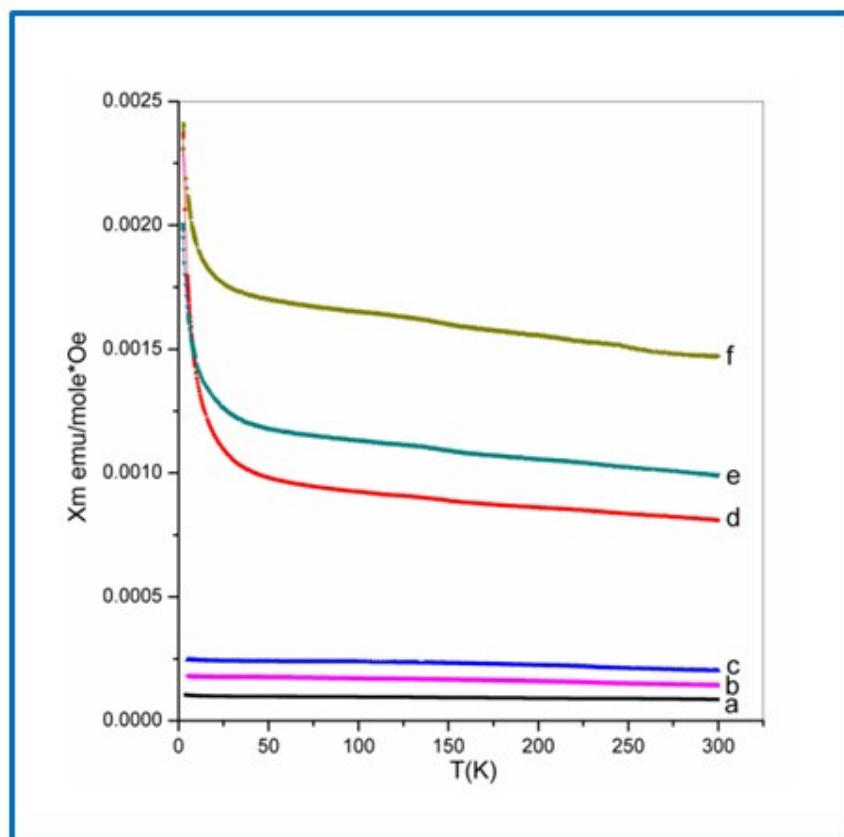


Figure 3B.9: Molar susceptibility vs. temperature plots in the range of 5K-300K of the complexes in free and encapsulated states (a) NiL1, (b) NiL6, (c) NiL4, (d) NiL1-Y, (e) NiL4-Y and (f) NiL6-Y.

Such alteration in the molecular orbitals leads to the radical change in magnetic behavior with enhanced magnetism of the guest complex compared to its free state. The comparative molar susceptibility data of NiL1-Y, NiL4-Y and NiL6-Y complexes are showing parallel pattern with the observed UV-Visible data as enhanced magnetization is maximum for NiL6-Y than NiL4-Y and then NiL1-Y complexes. It is reasonably clear that the observed blue

shift in the d-d bands assigned as d_z^2 - d_{xy} transitions, indicates the increase of energy gap in these two levels and it might be a reason for reduce the energy gap between d_{xy} - $d_{x^2-y^2}$ levels. As a result, the slightly higher lying excited triplet state becomes somewhat more accessible. NiL6-Y complex has a considerable fraction of the complex molecules to be present in high lying triplet energy states so as to contribute in enhanced magnetism. Similar behaviour is observed from other complexes, as NiL4-Y shows in-between and NiL1-Y shows comparatively lesser enhancement in magnetization.

3B.2.8. Theoretical Study

3B.2.8.1. Structure & Geometry

We have performed detailed theoretical studies for the NiL1, NiL4 and NiL6 complexes for a better evaluation of structural changes resulting drastic changes in optical and magnetic properties post encapsulation (details of methods are presented in Chapter 2 in section 2.3.9 under theoretical methods). The neat NiL1, NiL4 and NiL6 exist in their ground singlet states, however, there exists high energy triplet states with two unpaired electrons for all complexes studied. The energy differences calculated between the singlet state and the triplet state for NiL1 is 13.20 kcal, NiL4 is 14.12 kcal and 12.26 kcal for NiL6. The calculated spin densities on Ni atom for the triplet state is 1.57 [total moment: $2.37 \mu_B$, $(n(n+2))^{1/2}$, where n is number of unpaired electrons] for NiL1 and ~ 1.55 [total moment: $2.34 \mu_B$,)] for both NiL4 and NiL6 which is in line with experimental magnetic measurements. According to our experimental findings the high energy non planer triplet state predominates when encapsulated, which has also been observed in our earlier study (Discussed in Chapter 3A). The structural optimizations are carried out for NiL1, NiL4 and NiL6 complexes in the neat singlet states and then in zeolite encapsulated triplet states and the optimized structures are presented in Figure 3B.10 and the structural parameters have been tabulated in Table 3B.4. The end-to-end distance is well defined parameter for the neat singlet complexes only; however, the deformation and twisting around the metal centre of the complexes in the triplet states make the end-to-end distance an ill defined parameter. The end-to end distances for NiL1, NiL4 and NiL6 are 12.95, 14.53 and 15.12 Å respectively, due to the presence of substituents in NiL4 and NiL6. The measure of the twisting and non-planarity of the complexes can be understood from the O-Ni-N and C-Ni-C non-bonded angles (rectangular boxes as marked in Figure 3B.10), which generally decreases upon encapsulation.

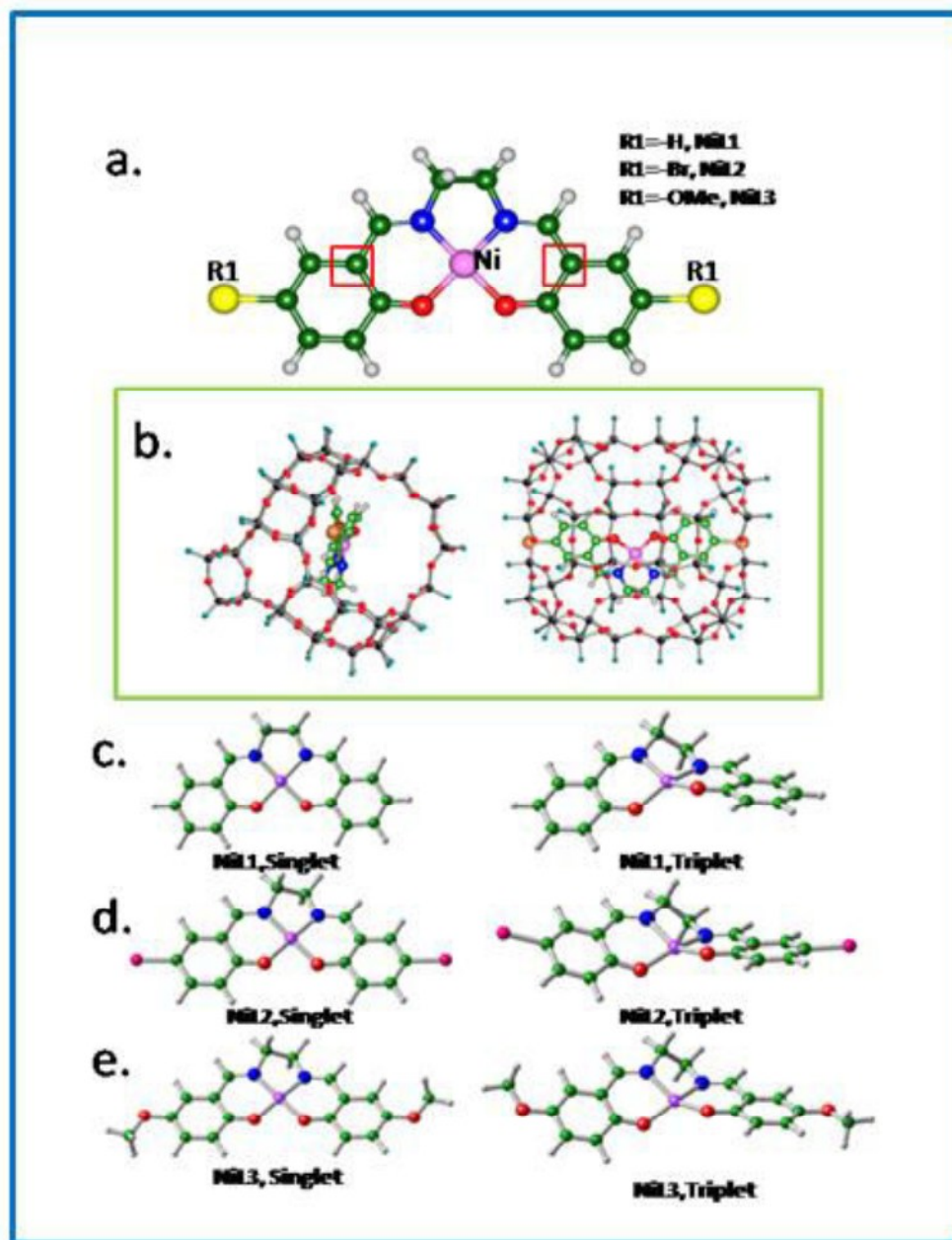


Figure 3B.10: Schematic structure for the Ni-salen complex in free state. b. Optimized structure of NiL6 (C atoms in green) encapsulated within zeolite supercage, two views are shown. Optimized structures of (c) NiL1, (d) NiL2 and (e) NiL3 in neat (singlet) state and encapsulated and extracted (triplet) states are shown.

In general, it is observed from the calculated Mulliken atomic charge distribution results, that the atomic charge increases when the complex is in the triplet state (encapsulated within

zeolite and is distorted) e.g., the Mulliken charge on Ni for NiL6 0.55 in neat state and 0.86 in encapsulated case with an increase in positive charge on the metal centre. Thus the experimental and theoretical studies show, in the free ground state, NiL1, NiL4 and NiL6 complexes are planar, diamagnetic and singlet, however, the complexes are deformed and twisted when encapsulated inside the zeolite pore and this deformation helps in the stabilization of the high energy triplet state. Which in turn alters the relative ordering of the molecular orbitals and consequently the magnetic behaviour.

Table 3B.4: Several important bond-distances, bond angles are reported for NiL1, NiL4 and NiL6 in the free and encapsulated cases. the end-to-end distances, HOMO and LUMO energies are also given.

Bond distances / angles	NiL1 free singlet	NiL4 free singlet	NiL6 free singlet	NiL1-Y encapsulated Triplet	NiL4-Y encapsulated triplet	NiL6-Y encapsulated triplet
Ni-O (Å)	1.84	1.84	1.84	1.88	1.89	1.88
Ni-N (Å)	1.85	1.85	1.85	1.96	1.96	1.98
O-C (Å)	1.30	1.29	1.29	1.30	1.29	1.29
N-C(conj) (Å)	1.30	1.30	1.30	1.29	1.30	1.30
<O-Ni-N	94	94	94.1	92.3	92.03	91.2
<C-Ni-C	179.8	179.7	179.8	169.7	167.2	171.5
End to end distance(Å)	12.95	14.53	15.12	13.15 (twisted)	14.7 (twisted)	15.54 (twisted)
HOMO (eV)	-5.29	-5.55	-4.91	-5.56, -5.83	-5.86, -6.04	-5.21, -5.30
LUMO(eV)	-1.83	-2.20	-1.78	-1.89, -2.30	-2.27, -2.70	-1.83, -2.22
HOMO-LUMO gap (eV)	3.46	3.35	3.13	3.67, 3.53	3.59, 3.34	3.38, 3.08

The switching of a diamagnetic planer molecule to a magnetic puckered molecule when encapsulated, thereby changing the optical and catalytic properties of the complexes is the focus of the present work. The nature of molecular orbital's of NiL1 and NiL3 complex is already discussed in chapter 3 and have shown in figure 3A.5. Our systematic studies (Tabulated in Table 3B.5) shows, the nature of the molecular orbitals are very similar for neat NiL4 and NiL6 complexes as well. The HOMO orbitals for the isolated NiL4 and NiL6

complexes have d_{xz} character and the LUMO orbitals have Ni d_{yz} character, both strongly hybridised with C p_z orbitals in the free singlet state. Similarly, HOMO-2 and LUMO+2 orbitals are mostly Ni d_z^2 and d_{xy} orbitals respectively. In the triplet state, the structural distortion of the complexes change the ordering as well as the energies of the molecular orbitals and the metal d orbitals are mostly affected as they are the frontier orbitals and the discussions of these MOs are given in the following section.

3B.2.8.2. Optical transitions from TD-DFT studies

TD-DFT methods are employed to calculate the UV-Vis spectra for the singlet states of the neat complexes and triplet states for the encapsulated NiL1, NiL4 and NiL6 complexes, as given in Figure 3B.11. The important d-d transitions calculated, with the corresponding energies, Oscillator strengths and assignments for the singlet states have been tabulated in Table 3B.6. We emphasize that in the triplet states of the complexes, the distortion around the metal centre mainly affects the Ni d orbitals and the forbidden d-d transitions (in neat singlet complexes) are no longer forbidden for the encapsulated complex; this is observed from broad and intense transitions experimentally. Interestingly, though the d-d transitions are affected by the encapsulation and distortion, they are more difficult to identify as the hybridisation of the metal d orbital with the ligand pi orbitals also increase strongly with distortion. The UV-Vis transitions devoid of strong Ni-d character remain unchanged after encapsulation and this is observed for the range of complexes studied. In case of neat NiL1, the first d-d transition is calculated at 615 nm, a transition primarily from HOMO orbital (Ni d_{xz}) \rightarrow LUMO+2 (Ni d_{xy} orbital) as shown in Table 3B.6. The transition around 538 nm occurring from HOMO-2 \rightarrow LUMO+2 is another important d-d transition (Ni d_z^2 to d_{xy} orbital). The transition around 477 nm occurring from HOMO-3 \rightarrow LUMO+2 is also a d-d transition (d_{yz} to d_{xy} orbital) mixed with effects from ligand orbitals. Next important transition is calculated at 436 nm (HOMO \rightarrow LUMO). In case of neat NiL4 and NiL6 the first two d-d transitions are identical in nature to that of the NiL1 complex and the results are tabulated in Table 3B.6. For NiL4, the peak at 617 nm, is a transition from HOMO (Ni d_{xz} orbital) \rightarrow LUMO+2 (mainly Ni d_{xy}), the transition at 540 nm occurs from HOMO-2 (Ni d_z^2) \rightarrow LUMO+2 (Ni d_{xy}) and, the transition from HOMO-3 (d_{yz}) \rightarrow LUMO+2 (d_{xy}) occurs around 475 nm. In case of isolated NiL6 complex, the d-d transitions are found at 636 nm, [HOMO (Ni d_{yz}) \rightarrow LUMO+2 (Ni d_{xy})], at 544 nm [HOMO-2 (Ni d_z^2) \rightarrow LUMO+2 (Ni d_{xy})]

and at 476 and 475 nm, HOMO(d_{xz}) \rightarrow LUMO(d_{yz}) transition with a comparatively higher oscillator strengths due to the mixing of HOMO-3 \rightarrow LUMO+2 transitions in different proportions.

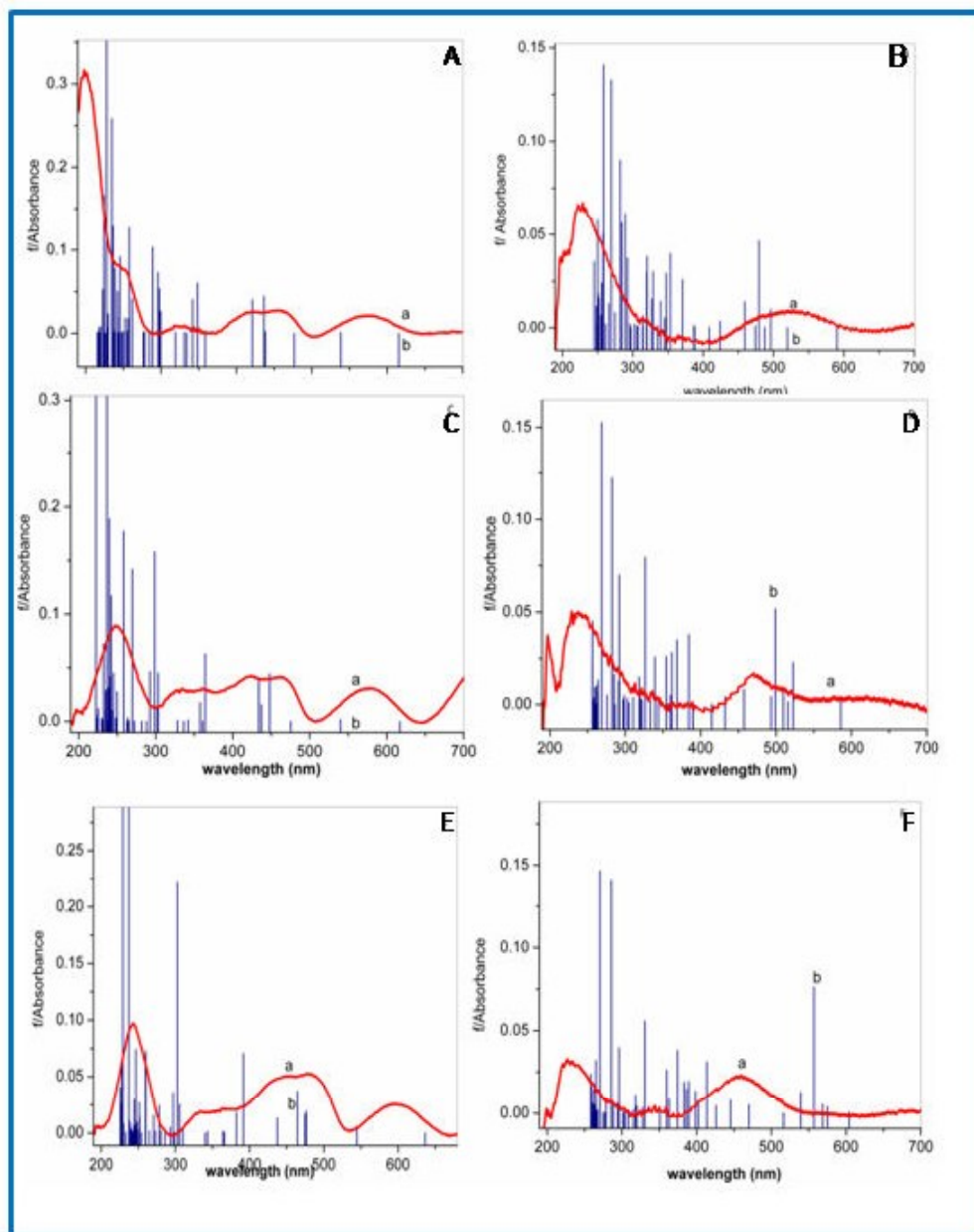


Figure 3B.11: Comparative UV-Visible data of (A-B) NiL1, (C-D) NiL4 and (E-F) NiL6 in free and encapsulated state, experimental data are represented by red line and TD-simulated data are represented by blue vertical line.

It must be noted that this value is much higher than NiL1 and NiL4 where this transition appears around 438 and 448 nm and not mixed with HOMO-3 \rightarrow LUMO+2 transitions. Next important transition for NiL6 is at 464 nm, a HOMO (d_{xz}) \rightarrow LUMO+1 (mainly ligand orbitals) a metal to ligand transition. One must note that the difference in the cases of NiL1, NiL4 and NiL6 are the effects of the substituents, which in spite of being far away from the metal centre, indirectly alter the electronic environment around it, and the effect of -OMe groups in the ligand is more drastic and the transitions are shifted to higher wavelengths. Even though the d-d transitions are difficult to identify in case of encapsulated triplet complexes, due to the increased hybridisation of ligand pi orbitals with the metal d orbitals, we have carefully tried to assign few important transitions.

Table 3B.5: Important d-d transitions, the energies, extinction coefficients and band assignments for NiL1, NiL4 and NiL6 in free, singlet case. The most important transition is given in bold and HOMO is abbreviated as H and LUMO is abbreviated as L.

Ni-Complex neat	Transitions (nm)	Energy (eV)	Oscillator strength (f)	Analysis of transitions
NiL1 (Singlet)	615	2.01	0.0000	H-0 \rightarrow L+2 , H-6 \rightarrow L+2
	538	2.30	0.0009	H-2 \rightarrow L+2 , H-0 \rightarrow L+0
	477	2.60	0.0001	H-3 \rightarrow L+2 , H-7 \rightarrow L+2,
	438	2.83	0.0022	H-5 \rightarrow L+2 , H-9 \rightarrow L+2
	436	2.84	0.0446	H-0 \rightarrow L+0 , H-2 \rightarrow L+2
NiL4 (Singlet)	617	2.01	0.0000	H-0 \rightarrow L+2 , H-4 \rightarrow L+2
	540	2.30	0.0017	H-2 \rightarrow L+2 , H-0 \rightarrow L+0
	475	2.61	0.0001	H-3 \rightarrow L+2 , H-7 \rightarrow L+2
	448	2.77	0.0446	H-0 \rightarrow L+0 , H-2 \rightarrow L+2
	437	2.84	0.0156	H-5 \rightarrow L+2 , H-13 \rightarrow L+2
NiL6 (Singlet)	636	1.95	0.0000	H-0 \rightarrow L+2 , H-4 \rightarrow L+2
	544	2.28	0.0046	H-2 \rightarrow L+2 , H-0 \rightarrow L+0
	476	2.60	0.0193	H-0 \rightarrow L+0 , H-3 \rightarrow L+2, H-2 \rightarrow L+2
	475	2.61	0.0167	H-0 \rightarrow L+0 , H-3 \rightarrow L+2, H-2 \rightarrow L+2
	464	2.67	0.0369	H-0 \rightarrow L+1
	437	2.84	0.0132	H-5 \rightarrow L+2 , H-11 \rightarrow L+2

The molecular orbitals of the encapsulated complexes are given in Appendix. For encapsulated NiL1 complex in triplet state, the first few transitions, partially involving metal

d-orbitals, become stronger and blue-shifted, however the $n-\pi^*$ bands and the $\pi-\pi^*$ remain unaltered. For triplet NiL1 the first d-d transition appears at 590 nm, a transition from inner HOMO-6 orbital (Ni d_z^2 with ligand orbitals) to LUMO+3 orbital (Ni d_{xy} orbital hybridized with O, N p orbitals). The moderately intense transition observed at 519 nm is a HOMO-2 (Ni d_{yz}) to LUMO+3 (Ni d_{xy}) transitions and is a d-d transition. The transition around 496 nm is from HOMO (primarily ligand based with Ni d_{xy}) to LUMO (primarily ligand based) which is mostly a ligand based transition. The intense transitions occurring at 480-420 nm are primarily intra ligand transitions with minimal involvement of metal d orbitals and correspond to the experimentally obtained $n-\pi^*$ bands. There are strong transitions observed around 320-350 nm which are $\pi-\pi^*$ transitions. For encapsulated NiL4 complex, the d-d transition appears at 586 nm which is a transition from HOMO-7 (Ni d_z^2 coupled with ligand orbitals) and HOMO-4 to LUMO+3 (Ni d_{xy} hybridized with O,N p orbitals) orbital and the transition around 523 nm HOMO-1 (Ni d_{xz}) to LUMO (Ni d_{xz} antibonding) are d-d transitions from beta orbitals. A transition around 515 nm is HOMO (d_{yz}) to LUMO (d_{xz}) transition from alpha orbital is also a d-d transition.

For triplet NiL6 complex, the d-d transition appears at 604 nm which is a transition from HOMO-7 orbital (Ni d_z^2 with ligand orbitals) to LUMO+3 orbital (Ni d_{xy} antibonding orbitals hybridized with O and N p orbitals) for beta orbitals and 575 nm a HOMO (Ni d_{xy}) to LUMO (Ni d_{yz}) transition for alpha orbitals. The strong peak around 557 nm involves orbitals which have small Ni d contributions, but the transition around 516 nm from HOMO (d_{yz}) to LUMO (d_{xy}) is a partial d-d transition. From the theoretical study of optical transitions, it is clear that after encapsulation, the d-d transition is shifted to lower wavelengths for all complexes, but the decrease is more for the substituted and encapsulated complexes. The $n-\pi^*$ and the $\pi-\pi^*$ transitions remain largely unaltered after encapsulation as even observed experimentally.

3B.2.9. Catalytic Activity

With the help of gas chromatography the catalytic activities of the complexes in neat as well as encapsulated states (Table 3B.6, GC chromatogram are given in Appendix A9- A17) have been studied for styrene oxidation reaction using H_2O_2 as oxidant. For this reaction, benzaldehyde is identified as major product in each of the cases whereas styrene oxide is minor product and phenylacetaldehyde is found in the trace amount. In the neat form, NiL4

shows maximum reactivity whereas NiL6 is merely reactive. It is quite obvious as the catalytic activity of the complexes are mainly driven by electronic factor of the substituent group present on the phenyl rings.⁴⁰ Presence of electron withdrawing group on phenyl rings makes the complex more active as catalyst for the oxidation reaction.⁷

Table 3B.6. Conversion of styrene after 8 hours reaction time with H₂O₂ as oxidant.

S.No	Samples	% Conversion	TON	Selectivity for bza	Selectivity for so
1	NiL1	13.5	108.64	51.61	48.38
2	ENiL1	4.51	89.6	96.74	3.25
3	NiL4	14.19	174	66.70	33.30
4	ENiL4	13.54	341	85.96	14.04
5	NiL6	9.67	92.32	89.09	10.91
6	ENiL6	16.72	375.9	87.75	12.25

Reaction conditions (Styrene: 1.56 g, 15 mmol), (H₂O₂: 3.40 g, 30 mmol), acetonitrile 15 ml, temperature 80⁰ C, and catalyst (0.075 g for encapsulated complexes and 0.006 g for neat complexes)TON (turn over number): mole of substrate converted per mole of metal center (encapsulated complexes).

In contrary, electron releasing group (-OCH₃) when attached on the phenyl rings, the complex loses its activity to a great extent. Therefore the observed trend of activity of the neat complexes towards the styrene oxidation reaction is just in accordance to the anticipation. However, in the encapsulated states, these complexes show diverse trend of reactivity from their corresponding neat states. These encapsulated systems are more selective for the benzaldehyde formation in comparison to their neat states. In the encapsulated states, NiL4 and NiL6 complexes are appeared to be more effective catalysts as compared to their corresponding neat forms as the turn over number (TON) for these

encapsulated systems are quite higher (Table 3B.6) whereas the behavior of NiL1 complex remains nearly unaltered. Comparative studies reveal that the NiL6 complex becomes the most effective catalyst under encapsulation though NiL4 complex in encapsulated state is showing quite a improved activity which finally leads to the decreasing order of catalytic activity as $\text{NiL6-Y} > \text{NiL4-Y} > \text{NiL1-Y}$.

These results indicate that after encapsulation the electronic factor is not as dominant as steric interaction between host and the guest which in turn imposes the host complex to adopt a distorted geometry. The most active NiL6-Y complex has been observed to undergo maximum extent of distortion as compared to NiL4-Y and NiL1-Y.

3B.2.9.1. Correlation between structural and functional alteration

Spectroscopic, magnetic and catalytic studies altogether provide enough evidences that the decreasing order of catalytic activity is just in accordance with the trend of extent of distortion experienced by these complexes on encapsulation. Comprehension of the adopted geometry of the guest complex under the steric constraints imposed by the host lattice and the change in functionality has been the exciting challenges. These Ni-complexes in their neat forms have a different activity trend as catalysts as NiL4 complex has greater reactivity than NiL1 and NiL6 complexes, because of electron withdrawing -Br group on phenyl rings, leads the electron deficiency on the nickel metal, and it makes the complex slightly distorted and more susceptible for nucleophilic attack of H_2O_2 . Whereas NiL6 complex has more electron density on the metal centre and is comparatively less reactive for nucleophilic attack than NiL4 and also NiL1 complex. After encapsulation the NiL6-Y complex endures more distortion from planarity and turns out to be the most reactive complex because of the removal of electron density from the the nickel centre due to the geometric distortion around the metal centre and becomes more susceptible for the nucleophilic attack of H_2O_2 . Theoretical study also supports this fact that after encapsulation the central metal atom of complex may have the more electropositive characters in comparison to its free state. The transition state, as a result becomes more stable, while electron rich nucleophile is bonded through the axial position.⁴⁰ NiL1 complex shows nearly a borderline behaviour in free state and being smallest in the lot, on encapsulation it undergoes minimum distortion as a result, it is least reactive for oxidation reaction after encapsulation in the zeolite Y.

3B.3. CONCLUSION

Above we present studies of square planar Ni(II)- complexes with various Schiff base ligands in free and encapsulated state. Modified functionalities offered by the various ligands evidently signify that the encapsulated complexes have adopted non planar geometry as a consequence while encapsulated, diamagnetic Ni(II) salen complexes act quite differently with enhanced magnetisation and also show significant blue shifts of the d-d transition. The observed optical, magnetic and catalytic behaviour are, however a consequence of distorted structure adopted by the complexes under encapsulation. Higher the molecular dimension, greater is the degree of distortion of the structure of the encapsulated complex as well as its catalytic activity.

REFERENCES

1. P. McMorn and G. J. Hutchings, *Chem. Soc. Rev.*, 2004, **33**, 108-122.
2. K. O. Xavier, J. Chacko and K. K. Mohammed Yusuff, *Appl. Catal., A*, 2004, **258**, 251-259.
3. M. R. Maurya, S. J. J. Titinchi, S. Chand and I. M. Mishra, *J. Mol. Catal. A: Chem.*, 2002, **180**, 201-209.
4. V. S. Marakatti and A. B. Halgeri, *RSC Adv.*, 2015, **5**, 14286-14293.
5. M. Salavati-Niasari, M. Shaterian, M. R. Ganjali and P. Norouzi, *J. Mol. Catal. A: Chem.*, 2007, **261**, 147-155.
6. J. H. Lunsford, W. P. Rothwell and W. Shen, *J. Am. Chem. Soc.*, 1985, **107**, 1540-1547.
7. S. Deshpande, D. Srinivas and P. Ratnasamy, *J. Catal.*, 1999, **188**, 261-269.
8. N. Y. Chen and W. E. Garwood, *J. Catal.*, 1978, **52**, 453-458.
9. K. Mori and H. Yamashita, *Chem. Eur. J.*, 2016, **22**, 11122-11137.
10. N. Herron, *Inorg. Chem.*, 1986, **25**, 4714-4717.
11. C. R. Jacob, S. P. Varkey and P. Ratnasamy, *Microporous Mesoporous Mater.*, 1998, **22**, 465-474.
12. R. F. Parton, I. F. J. Vankelecom, M. J. A. Casselman, C. P. Bezoukhanova, J. B. Uytterhoeven and P. A. Jacobs, *Nature*, 1994, **370**, 541-544.
13. Y. Umemura, Y. Minai and T. Tominaga, *J. Phys. Chem. B*, 1999, **103**, 647-652.
14. S. Ray and S. Vasudevan, *Inorg. Chem.*, 2003, **42**, 1711-1719.

15. P.-P. Knops-Gerrits, D. De Vos, F. Thibault-Starzyk and P. A. Jacobs, *Nature*, 1994, **369**, 543-546.
16. M. Salavati-Niasari, *J. Mol. Catal. A: Chem.*, 2008, **284**, 97-107.
17. M. Salavati-Niasari, M. Shakouri-Arani and F. Davar, *Microporous Mesoporous Mater.*, 2008, **116**, 77-85.
18. M. Salavati-Niasari and A. Sobhani, *J. Mol. Catal. A: Chem.*, 2008, **285**, 58-67.
19. M. J. Sabater, A. Corma, A. Domenech, V. Fornes and H. Garcia, *Chem. Commun.*, 1997, DOI: 10.1039/A701337J, 1285-1286.
20. Y. Yu, J. Mai, L. Wang, X. Li, Z. Jiang and F. Wang, *Sci. Rep.*, 2014, **4**.
21. S. K. Tiwary and S. Vasudevan, *Inorg. Chem.*, 1998, **37**, 5239-5246.
22. K. K. Bania and R. C. Deka, *J. Phys. Chem. C*, 2012, **116**, 14295-14310.
23. W. H. Quayle, G. Peeters, G. L. De Roy, E. F. Vansant and J. H. Lunsford, *Inorg. Chem.*, 1982, **21**, 2226-2231.
24. W. H. Quayle and J. H. Lunsford, *Inorg. Chem.*, 1982, **21**, 97-103.
25. K. K. Bania, D. Bharali, B. Viswanathan and R. C. Deka, *Inorg. Chem.*, 2012, **51**, 1657-1674.
26. M. Jafarian, M. Rashvand avei, M. Khakali, F. Gobal, S. Rayati and M. G. Mahjani, *J. Phys. Chem. C*, 2012, **116**, 18518-18532.
27. G. Ramanjaneya Reddy, S. Balasubramanian and K. Chennakesavulu, *J. Mater. Chem. A*, 2014, **2**, 15598-15610.
28. A. R. Silva, M. Martins, M. M. A. Freitas, A. Valente, C. Freire, B. de Castro and J. L. Figueiredo, *Microporous Mesoporous Mater.*, 2002, **55**, 275-284.
29. J. G. Dillard and L. T. Taylor, *J. Electron. Spectrosc. Relat. Phenom.*, 1974, **3**, 455-460.
30. L. J. Matienzo, W. E. Swartz and S. O. Grim, *Inorg. Nucl. Chem. Lett.*, 1972, **8**, 1085-1091.
31. K. K. Bania and R. C. Deka, *J. Phys. Chem. C*, 2013, **117**, 11663-11678.
32. B. Dutta, S. Jana, R. Bera, P. K. Saha and S. Koner, *Appl. Catal., A*, 2007, **318**, 89-94.
33. M. Asadi, K. A. Jamshid and A. H. Kyanfar, *Inorg. Chim. Acta*, 2007, **360**, 1725-1730.
34. K. K. Bania, D. Bharali, B. Viswanathan and R. C. Deka, *Inorg. Chem.*, 2012, **51**, 1657-1674.

35. L. Gomes, E. Pereira and B. de Castro, *J. Chem. Soc., Dalton Trans.*, 2000, DOI: 10.1039/A908330H, 1373-1379.
36. N. Grover, M. Sankar, Y. Song and K. M. Kadish, *Inorg. Chem.*, 2016, **55**, 584-597.
37. S. Di Bella, I. Fragala, I. Ledoux, M. A. Diaz-Garcia, P. G. Lacroix and T. J. Marks, *Chem. Mater.*, 1994, **6**, 881-883.
38. H. Yoon, T. R. Wagler, K. J. O'Connor and C. J. Burrows, *J. Am. Chem. Soc.*, 1990, **112**, 4568-4570.
39. J. E. Reed, A. A. Arnal, S. Neidle and R. Vilar, *J. Am. Chem. Soc.*, 2006, **128**, 5992-5993.
40. M. M. Bhadbhade and D. Srinivas, *Inorg. Chem.*, 1993, **32**, 6122-6130.



Chapter 3: Part C

**The Effect of the Molecular Dimension of the
Nickel Salen Complex on its Functionality after
Encapsulation in zeolite Y**

3C.1. INTRODUCTION

Earlier we have reported that the diamagnetic nickel Schiff-base complex when encapsulated in zeolite Y, adopts the non-planar geometry due to space constraint where nickel metal is out of the plane of N_2O_2 moiety, exhibiting paramagnetism. However the same complex, when encapsulated in another host with much larger pore diameter such as MCM-41, doesn't manifest this behaviour (Discussed in chapter 3A). In addition to the study we have also observed that the nickel (II) Schiff-base complexes having different molecular dimensions when encapsulated within the zeolite supercage, higher the molecular dimension of the complex, greater is the degree of distortion of the structure and better is the catalytic activity. In extension of previous work, we have synthesized the nickel Schiff base complex (N, N'-bis(4-hydroxy salicylidene)ethylenediamine as NiL2) with nearly same 'end-to-end' distance ($\sim 12.98 \text{ \AA}$) of nickel salen (NiL1) complex (Which is discussed in chapter 3B) encapsulated within the supercage of zeolite-Y with a pore diameter of 12.47 \AA via flexible ligand synthesis method. However the complex has two hydroxyl groups on the 4th positions of phenyl rings of the ligand, which doesn't have contribution to make its bigger in terms of end-to-end-distance but it surely makes it larger in other dimension (given in Figure 3C.1.) compared to the NiL1 complex which doesn't have any substituent on it. Therefore the difficulty still lies into how to fit the planar complex into the spherical cavities of zeolite-Y. We have carried out the detailed characterization of the system with the help of comparative spectroscopic (IR, UV-Vis), morphological (XRD, SEM), magnetic and theoretical studies to understand the confinement of the complex in zeolite Y supercage.

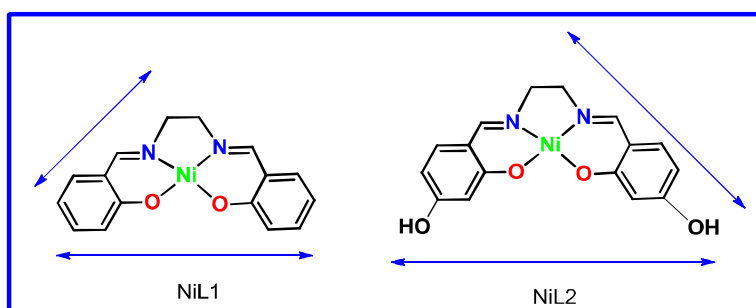


Figure 3C.1: Comparative molecular dimensions of NiL1 and NiL2 complexes.

DFT studies have provided the detailed information of different adopted geometries of the guest complexes under space constraint within zeolite. Furthermore, optical spectra are

simulated employing TD-DFT method to have a greater insight of the experimentally observed shifts in UV-Vis spectra of the zeolite encapsulated complexes. Additionally, we have employed complex as catalyst both in free and entrapped states on the styrene oxidation reaction to comprehend the extent of distortion and modified reactivity of the complexes after encapsulation in zeolite Y.

3C.2. RESULT AND DISCUSSIONS

Synthesis of complex in free as well as in the encapsulated state of zeolite Y has been accomplished via flexible ligand synthesis method (already discussed in chapters 2 under experimental methods 2.1-2.6).

3C.2.1. Powder XRD Analysis

The powder X-ray diffraction patterns of Na- zeolite Y, Ni- zeolite Y, and NiL2-Y complex in zeolite Y systems are shown in Figure 3C.2. The powder XRD pattern of NiL2 is essentially similar with that of the pure and nickel exchanged zeolite Y, indicating the retention of integrity of host zeolite lattice after the encapsulation processes. However the noticeable intensity reversal observed at $2\theta = 10^\circ$ and 12° positions in the XRD patterns for the encapsulated complex probably ensures the encapsulation.

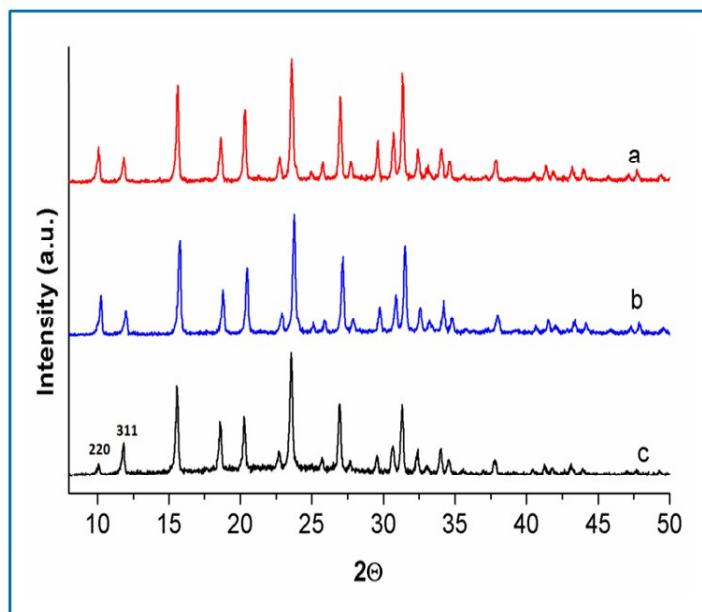


Figure 3C.2: Powder XRD patterns of (a) pure zeolite-Y (b) Ni exchanged zeolite-Y (c) NiL2-Y

Pure and nickel exchanged zeolite Y hold the intensities relation as $I_{220} > I_{311}$, whereas after

the encapsulation of a large complex within the supercage, the XRD pattern of the hybrid system holds the reverse relation of intensities as $I_{220} < I_{311}$. In the literature, empirical correlation of such observation with the presence of a large complex inside the supercage of zeolite Y already exists.¹⁻⁴ Such type of experimental observation does not appear in case of tethering of complex and even if complex does not form in the cavity of supercage.^{5, 6} Furthermore, appearance of any extra peak is not observed as expected because the loading levels of the metal complex maintained in zeolite are very low.

3C.2.2. Elemental Analysis

The parent host material, Na-zeolite Y has the unit cell formula as $\text{Na}_{58}\text{Al}_{58}\text{Si}_{136}\text{O}_{388} \cdot y\text{H}_2\text{O}$ and Si/Al ratio is 2.34. EDS spectra and data of NiL2-Y [Appendix A6] suggests that Si/Al ratio remains unaffected, which signifies that the leaching of aluminium doesn't take place during encapsulation processes. Presence of both the sodium and nickel metal ions, in the hybrid system of zeolite with the encapsulated complex within indicates the partial exchange of sodium metal ions during exchange reactions. The nickel ion concentration in encapsulated complex is observed to be lesser than that in nickel exchanged zeolite Y as expected because of possible leaching of some of the metal ions during the synthesis of complex which in turn, can lead in lowering the nickel ion concentration. The general formula of Ni-exchanged zeolite-Y sample is $\text{Ni}_x\text{Na}_{58-2x}\text{Al}_{58}\text{Si}_{136}\text{O}_{388} \cdot y\text{H}_2\text{O}$. In the present study the nickel metal concentration is (0.50) wt % for the NiL2-Y.

3C.2.3. Scanning Electron Microscopy Analysis

Encapsulation of metal complex within the supercage of zeolite-Y essentially targets the complex formation only inside the cavities of supercage, however such a precise method of surface of zeolite lattice have been removed by extensive Soxhlet extraction. synthesis not feasible practically. Inevitable adsorptions of some complexes and ligand on the surface of zeolite lattice have been removed by extensive Soxhlet extraction. SE micrographs of pure zeolite Y, NiL2-Y after Soxhlet extraction is shown (Figure 3C.3a-b). After Soxhlet extraction, surface boundaries of host lattice are much clearly visible and differentiable, providing a clear indication of the removal of surface species from surface, as well as preservation of crystallinity of zeolite framework.^{3, 7} Eventually the SEM analysis gives the indirect evidence about the complex formation, mostly occurring inside the host cavity only.

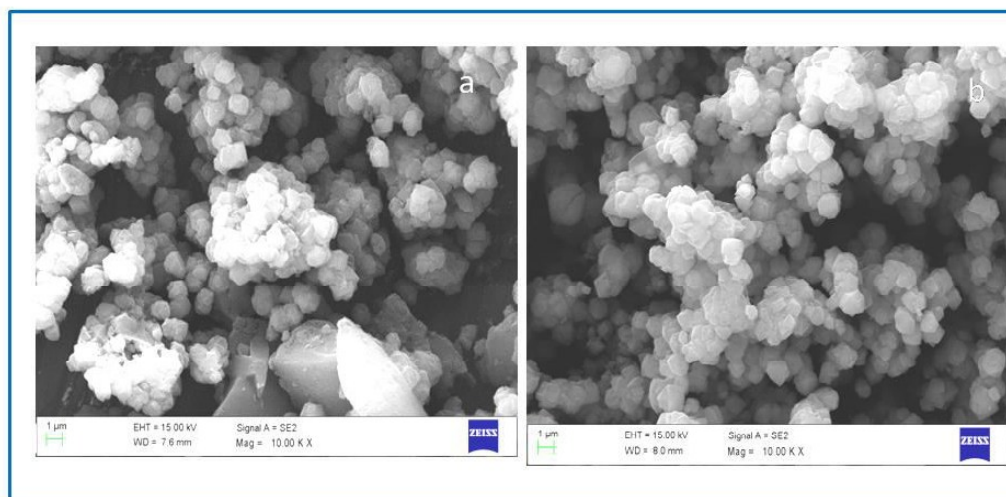


Figure 3C.3: SEM images of (a) pure zeolite Y, (b) NiL2-Y after Soxhlet extraction.

3C.2.4. X-Ray Photoelectron Spectroscopy

The existence of metal complex in the zeolite framework has been further confirmed by the X-ray photoelectron spectroscopy (XPS). The survey spectra and high resolution XP spectra of C (1s), N (1s), O (1s) and Ni (2p) of NiL2-Y are presented in Figure 3C.4. The observed spectra and binding energy data (Figure 3C.4 and Table 3C.1) clearly indicates the presence of C, N, O, Na, Si, Al, Ni(II) in their respective chemical states, which is accordance to the literature.⁸⁻¹² The loading level of metal is low in the complex within the host lattice, therefore the weak XPS peak intensities are observed for nickel (2p) signals for the encapsulated complex (NiL2-Y) and it is perfectly in agreement with the other concentration dependent studies obtained from EDX, IR and UV-Visible spectroscopies. It already has been observed that Ni-salen in both its free and zeolite encapsulated forms show the appearance of $2p_{3/2}$ and $2p_{1/2}$ peaks in the XPS spectra at the binding energies at around 855 and 872 eV suggesting nickel metal present in +2 oxidation state in both the forms. As well as absence of any shake up and satellite peak around 878 eV confirms that the complex stays in square planar geometry not in the octahedral geometry.^{8, 11} Intense and broad carbon (1s) XPS spectra have observed for nickel salen complex in both states which further deconvoluted into two peaks and validated the presence of sp^3 and sp^2 carbon atoms in complex. Similarly the

complex have shown the nitrogen (1s) and oxygen (1s) XPS traces for (M-N), (N=C) and (C-O), (M-O) respectively.

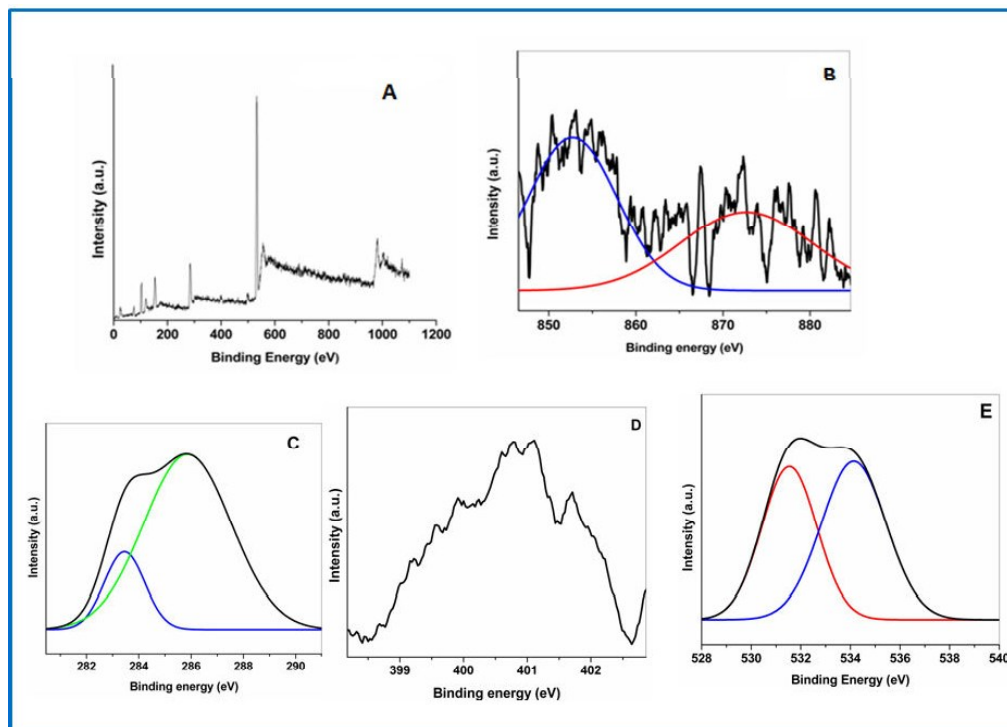


Figure 3C.4: XPS spectra of NiL2-Y complex (A) survey spectra, High resolution XPS spectra of (B) nickel (2p), (C) carbon (1s), (D) nitrogen (1s) and (E) oxygen (1s). (Black colored graphs are experimental data and green and blue colored peaks are peak fitted data)

Table 3C.1: Binding energy of the neat and encapsulated complex.

S.No	Sample	Si (2p)	Al (2p)	C (1s)	N(1s)	O (1s)	Ni ²⁺ (2p)
1.	NiL2-Y	103.50	75.60	285.79 283.43	399.67, 400.92	534.1, 531.1	853.40, 872.95

In the present study, encapsulated NiL2-Y also has shown the essentially similar patterns of XPS signals for all constituent atoms of the complex with the minor shifts in the signals. The encapsulated NiL2-Y complex has demonstrated $2p_{3/2}$ and $2p_{1/2}$ peaks at 853.40 and 872.95 eV binding energies since Ni in the complex is present in +2 oxidation state with square planar geometry. Furthermore, carbon (1s) XPS spectra of NiL2-Y have confirmed the presence of sp^3 and sp^2 carbon atoms and XPS traces of nitrogen (1s) are deconvoluted into

two signals associated to (M-N) and (N=C) peaks. Oxygen (1s) XPS traces are deconvoluted into two peaks which are attributed to (M-O) and (C-O) peaks. All observed signals along with the Si (2p) and Al (2p) peaks in NiL2-Y hybrid system are in accordance with the literature. Presence of all elements in the expected chemical states and nickel metal ion in +2 oxidation state undeniably signifies the successful formation of NiL2-Y within the supercage of zeolite-Y.

3C.2.5. Infrared Spectroscopy

The IR spectra of pure zeolite Y, NiL2, and NiL2-Y are shown in Figure 3C.5, and corresponding data are provided in the Table 3C.2. Pure-zeolite-Y mainly shows major characteristics bands in the region of 450-1200 cm^{-1} and also at around 1643 cm^{-1} and 3500 cm^{-1} region which already have been discussed in previous chapters (3A and 3B). The appearance of these zeolitic bands even for the integrated host-guest systems (Figure 3C.5) indicate the preservation of host lattice integrity, during the process of encapsulation. However, the characteristic IR bands of the encapsulated complexes are majorly masked by strong zeolitic bands over most of the range.

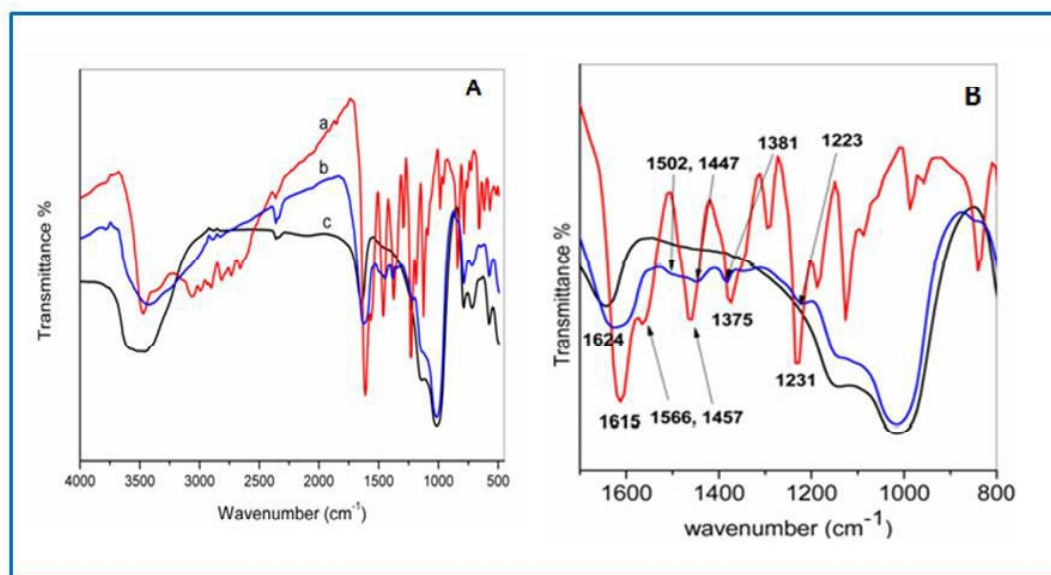


Figure 3C.5: (A) FTIR spectra in the range of 500 cm^{-1} to 4000 cm^{-1} of (a) NiL2 (b) NiL2-Y, and (c) pure zeolite Y. (B) magnified view of IR data of (a) NiL2 (b) NiL2-Y, and (c) pure zeolite Y.

Table 3C.2: IR spectral data (cm^{-1}) of neat and encapsulated complexes.

S.No	Samples	$\nu_{\text{(C=N)}}$ stretching	$\nu_{\text{(C=C)}}$ stretching	$\nu_{\text{(C-H)}}$ deformation	$\nu_{\text{(C-O)}}$ stretching
1.	NiL2	1613	1566, 1457	1375	1231
2.	NiL2-Y	1624	1502, 1447	1381	1223

The signal intensity is very low, because of very low concentration of metal complex inside the framework, the only region of $1600\text{-}1200\text{ cm}^{-1}$ is found to be suitable for the study because in that region bands appear only from the guest complex; Within $1600\text{-}1200\text{ cm}^{-1}$, encapsulated complex shows main characteristics C=C, C=N and C-O stretching¹³ and C-H deformation bands with small shifts. The shift in these bands can be due to the different environment imposed by the cavity on the of guest complex. The C-H deformation band of the complex has shifted from 1375 cm^{-1} to 1381 cm^{-1} under encapsulation.¹⁴ These observed IR data point towards the successful synthesis of the nickel Schiff-base complex inside the pores of zeolite-Y. The overall experimental FTIR spectral data (Table 3C.2) suggests the successful synthesis of the complex in the 'free' as well as in encapsulated state inside the zeolite Y cavities.

3C.2.6. UV-Visible Spectroscopy

Electronic spectra of the L2 ligand and 'free state' NiL2 complex have been recorded in chloroform (Given in Figure 3C.6). Chloroform is preferred over the other solvents because it is already an established fact that in chloroform, such complexes experience minimum structural deviation from planarity when dissolved in chloroform.¹⁵ The comparative solid state UV-Vis studies of the complex in 'free state' complex and zeolite entrapped state have been carried out (shown in Figure 3C.6 and Table 3C.3) to explore the change of electronic environment around the metal centre after encapsulation. Not only that, comparative studies of this system with those of NiL1 become relevant in this point to investigate the effect of the substituent groups. The free state complexes NiL1, NiL2) show the high energy strong bands at 251 nm and 241 nm respectively, which are attributed to $\pi\text{-}\pi^*$ transitions. Further two bands at 323 and 413 nm in the spectrum of NiL1, and at 325 nm and 397 nm in the spectrum

of NiL2 are the $n-\pi^*$ transitions.⁷ For both NiL1 and NiL2, relatively weak yet broad absorption bands adjacent to $n-\pi^*$ bands, at 453 nm and 439 nm respectively must have originated from charge transfer transitions. The broad d-d band centred at $\sim(555-570)$ nm for NiL1 and $\sim(560-580)$ nm for NiL2 can be attributed majorly to the transition from d_z^2 to d_{xy} orbital.¹⁶ The appearance of charge transfer bands and d-d bands directly proves the formation of the complex. The UV-Vis spectral bands of encapsulated complexes are not so distinctly visible, due to very low concentration of complex inside zeolite, but it is quite apparent that, the high energy $\pi-\pi^*$ and $n-\pi^*$ transitions for both the encapsulated complexes occur nearly same positions as their corresponding 'free state' complexes. However on encapsulation, lower energy d-d bands, are considerably intensified¹⁴ and blue shifted with respect to the corresponding 'free state' d-d bands. Such type of electronic behaviour reveals that the complex is not able to sustain its planar geometry especially around the metal ion due to space restrictions imposed by the host cavity.

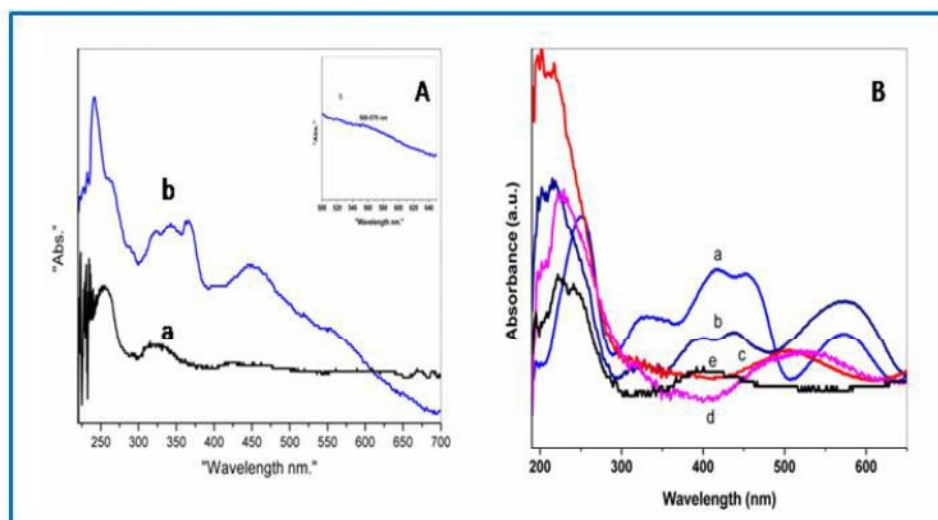


Figure 3C.6: (A) UV-Vis spectra in chloroform in the range of 190-700 nm of (a) L2 and (b) NiL2. (B) Solid state UV-Vis spectra in the range of 190-700 nm of (a) NiL1 (b) NiL2 (c) NiL2-Y and (d) NiL1-Y.

Though both NiL1 and NiL2 complexes have nearly same end-to-end distances as 12.94\AA and 12.99\AA respectively, two hydroxyl substituents on both the phenyl rings of NiL2 complex lead in increase of the width of the complex essentially requiring more space to be accommodated inside the nearly spherical supercage (cavity diameter is 12.47\AA). The extent of observed blue shift in d-d bands is roughly double for NiL2 as compared to that of

NiL1 under entrapment. The observed blue shift in the d-d band of NiL1-Y is around 30 nm, whereas that in NiL2-Y is approximately 65-70 nm. The observed blue shift definitely in turn points towards the reduction of the gap between d_{xy} and $d_{x^2-y^2}$ orbitals.

Table 3C.3: Solid state UV-Vis spectral data of “neat” and encapsulated complexes.

S.No	Samples	$\pi-\pi^*$ Transiti	$n-\pi^*$ Transition	CT Transition	<i>d-d</i> Transition
1.	NiL1	251	323, 355	413,453	565-570
2.	NiL1-Y	242	320, 360		530-540
3.	NiL2	241	325, 397	439	570-580
4.	NiL2-Y	237	324, 382		495-505

This observation is in line with the argument that extent of distortion in the case of entrapped NiL2 complex is more than that for NiL1 complex under confinement. It is explicable, as the complex with comparatively bulkier ligand experiences more space constraint, imposed by the host framework, which makes the complex more distorted and is also well supported by the electronic spectroscopic studies.

3C.2.7. Theoretical Studies & Results

As described in the previous sections, we have performed detailed theoretical studies (methodology in Chapter 2) on NiL1 and NiL2 complexes in isolated, singlet and encapsulated triplet forms.

3C.2.7.1. Structure & Geometry

The ground states of NiL1 and NiL2 salen complexes are planar, diamagnetic and exist as singlet states without any unpaired electrons. The structure of the NiL1 and NiL2 complexes in the free state and then in zeolite encapsulated triplet states are relaxed and the optimized structures are presented in Figure 3C.7. The structure of the encapsulated complexes shows deviations from those of the neat complexes and few important results have been tabulated in Table 3C.4. The variations in the bond distances and bond angles upon encapsulation are small and are due to the influence of the zeolite framework, however, the NiL1 and NiL2

complexes as a whole are deformed and puckered when packed inside the pore. The encapsulation process changes the ordering of the molecular orbitals in such a way that the magnetic triplet state becomes stable. The switching of a diamagnetic planar molecule to a magnetic puckered molecule when encapsulated is the focus of the present work. The neat NiL1 and NiL2 complexes though are planar, diamagnetic and are more stable in singlet states, they may also exist in high energy triplet states with two unpaired electrons.

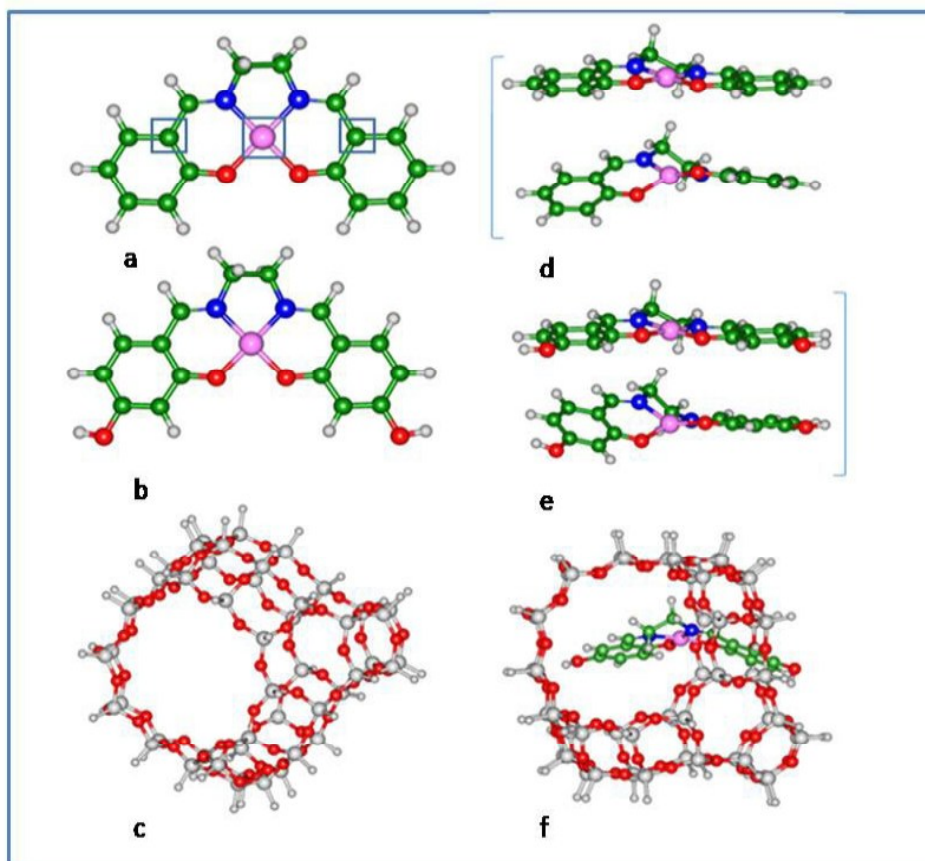


Figure 3C.7. (a) NiL1 (singlet) free state (b) NiL2 free singlet state. The atoms marked by the squares define the C-Ni-C bond angle in different molecules. (c) The zeolite framework used for theoretical studies. (d) The deformation of encapsulated Ni-salen (bottom) shown with respect to its neat form (top). (e) The deformation of NiL2-Y (bottom) shown with respect to its neat form (top). (f) NiL2-Y molecule (triplet)

The energy differences calculated between the singlet state and the triplet state for free neat NiL1 is 12.8 kcal and 11.8 kcal for NiL2. The non planar triplet state predominates when encapsulated as the experimental magnetic studies indicate. The theoretical spin densities on

Ni atom is 1.56 (total moment: $2.35 \mu\text{B}$, $[\text{n}(\text{n}+2)]^{1/2}$, where n is number of unpaired electrons) for NiL1 and 1.68 (total moment: $2.49 \mu\text{B}$) for NiL2. From the results tabulated in Table 3C.4, we find that bond distances Ni-N distances change when encapsulated both for NiL1 and NiL2. The O-C and N-C distances are unchanged for both free and encapsulated cases of NiL1 and NiL2. The bond angles O-Ni-N and C-Ni-C (atoms shown in rectangular boxes as marked in Figure 3C.7, give an idea about the non-planarity of the molecule), changes for both complexes after encapsulation.

Table 3C.4: Important geometrical parameters and molecular orbital's for NiL1 and NiL2 in free and encapsulated case (B3LYP/6-31++G**).

Bond distances / angles	NiL1 free singlet	NiL2 free singlet	NiL1-Y encapsulated Triplet	NiL2-Y encapsulated triplet
Ni-O (A)	1.85	1.85	1.88	1.89
Ni-N (A)	1.87	1.87	1.96	1.97
O-C (A)	1.30	1.29	1.30	1.29
N-C(conj) (A)	1.30	1.30	1.29	1.30
<O-Ni-N	93.9	93.9	92.3	92.22
<C-Ni-C	179.9	179.9	169.8	169.3
End to end distance (A)	12.98	12.99	13.15 (twisted)	13.25
HOMO (eV)	-5.28	-5.26	-5.53, -5.79	-5.51, -5.79
LUMO(eV)	-1.83	-1.60	-1.86, -2.32	-1.66, -2.24
HOMO-LUMO gap (eV)	3.45	3.66	3.67, 3.47	3.85, 3.55

The HOMO for neat NiL1 has a d_{yz} character hybridized with the p bonding character of the salen ligand, and the LUMO has Ni d_{xz} character hybridised with p antibonding type orbitals from C and N. The HOMO and LUMO energies are -5.28 and -1.83 eV respectively with a HOMO-LUMO energy gap of 3.45 eV. The overall distortion of the complex NiL2 after encapsulation is indicated from the same bond-angles O-Ni-N; which changes from 93.9° to 92.2° and C-Ni-C which changes from 179.99° to 169.3° . The HOMO for the isolated NiL2 complex has a d_{yz} character and the LUMO has Ni d_{xz} character. The HOMO and LUMO energies are -5.26 and -1.60 eV respectively with a HOMO-LUMO energy gap of 3.66 eV.

The change in the bond distances and bond angles on encapsulation may be attributed to the influence of the zeolite framework, where the zeolite valence electrons are distributed all over as a delocalized electron cloud and interacts strongly with the encapsulated Ni complex.

3C.2.7.2. Optical transitions from TD-DFT studies

TD-DFT methods are employed to calculate the UV-Vis spectra for the singlet states of the neat complexes and triplet spin states for the encapsulated NiL1 and NiL2 complexes, as given in Figure 3C.8 and some selected d-d transition are listed in Table 3C.5.

Table 3C.5: Important selected electronic transition of NiL1 and NiL2 in free and encapsulated case.

Samples	Transitions (nm)	Analysis of transitions
NiL1	633	HOMO (Ni d_{yz}) \rightarrow LUMO+2 (Ni d_{xy} hybridized with O and N p orbitals)
	555	HOMO-2(Ni d_z^2) \rightarrow LUMO+2(Ni d_{xy})
	493	HOMO-3 (Ni d_{yz}) \rightarrow LUMO+2 (Ni d_{xy})
NiL1-Y	589	HOMO-6 orbital (Ni d_z^2) \rightarrow LUMO+3 orbital (Ni d_{xy}).
	499	HOMO-1 \rightarrow LUMO
NiL2	627	HOMO (Ni d_{yz}) \rightarrow LUMO+2 (Ni d_{xy} hybridized with O and N p orbitals)
	556	HOMO-4(Ni d_z^2) \rightarrow LUMO+2(Ni d_{xy})
NiL2-Y	596	HOMO-6 orbital (Ni d_z^2) \rightarrow LUMO+3 orbital (Ni d_{xy} hybridized with O and N p orbitals)
	475	HOMO-1 \rightarrow LUMO

In NiL1, strong bands around 420 and 350 nm are due to transitions; HOMO to LUMO+1, HOMO-2 to LUMO and HOMO-1 to LUMO respectively which could correspond to the $n-\pi^*$ bands as observed experimentally. Several intra ligand charge transfer bands ($\pi-\pi^*$) are calculated around 280 nm. In case of NiL1-Y The intense transitions occurring at 450-390

nm (HOMO to LUMO, HOMO-1 to LUMO, HOMO to LUMO+1 orbitals) are primarily intra ligand transitions with minimal involvement of metal d orbitals and correspond to $n-\pi^*$ bands experimentally.

In case of isolated NiL2 complex, Ligand to metal charge transfer transition is calculated at 451 nm (HOMO-5 to LUMO+2) and at 396 nm the transition from HOMO to LUMO+1 is an intra ligand transition. Strong transitions around 340-310 nm are $n-\pi^*$ transitions. Several $\pi-\pi^*$ bands occur around 270 nm. For encapsulated NiL2 complex, moderately intense transitions are observed at 475, 462 nm which are HOMO-1 to LUMO and HOMO-4 to LUMO+3 for beta orbitals, which are mainly ligand to metal charge transfer transition.

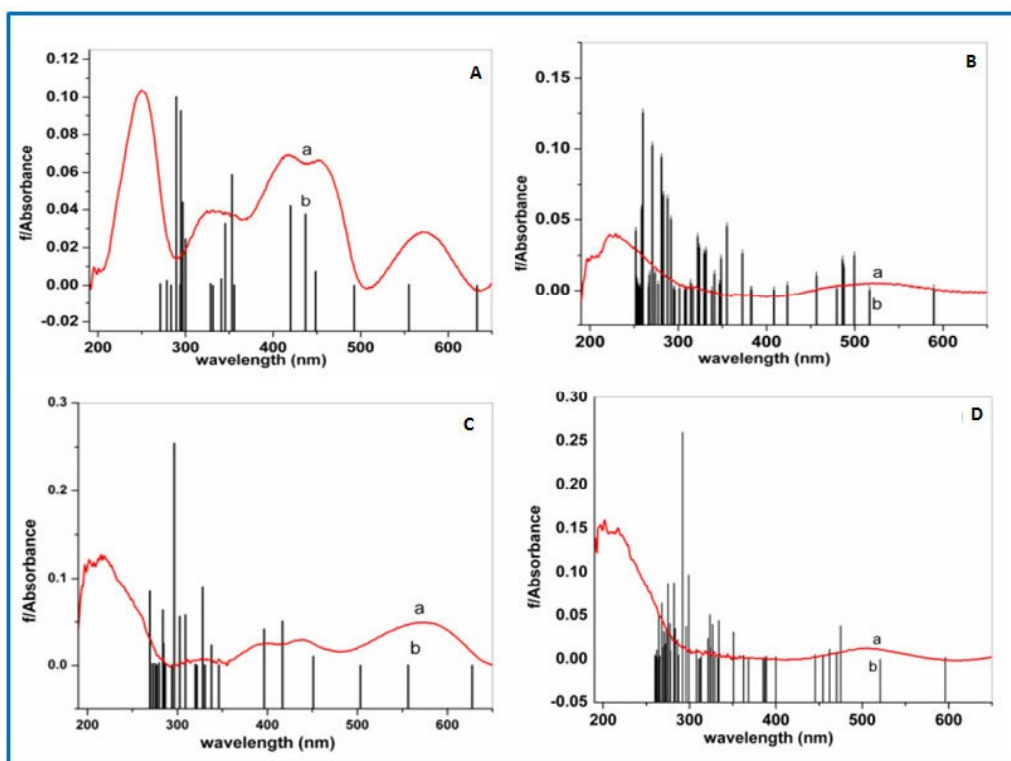


Figure 3C.8: Comparative UV-Visible data of (A) NiL1 (B) NiL1-Y (C) NiL2 and (D) NiL2-Y experimental data are represented by red line and TD-simulated data are represented by black vertical line.

Theoretically there are intense transitions occurring at 350-320 nm are primarily intra ligand transitions with very small involvement of metal d orbitals. Theoretically intense $\pi-\pi^*$ intra ligand transitions occur around 270-290 nm for both complexes.

3C.2.8. Magnetic Studies

Optical spectroscopic studies as well as the theoretical studies clearly indicate the distortion in geometry of NiL2 complex upon encapsulation, therefore to comprehend the geometry adopted by the encapsulated complex especially around the metal centre, magnetic studies have been carried out and then compared with that of NiL1 (without any substitution) entrapped in zeolite-Y. The planar d^8 nickel complexes are diamagnetic. Several literature reports are available, which clearly suggest that these metal complexes are diamagnetic in nature, without any effect of the substituent on the benzene rings.¹⁷⁻¹⁹ From the observed experimental magnetic data in the temperature range of 4K-300K, the NiL1 complex, is found to be almost diamagnetic with magnetic moment near to zero (0.45 BM), which essentially indicate planarity of N_2O_2 moiety around the Ni(II) centre.¹⁷ However, in the same temperature range, both the encapsulated NiL1-Y and NiL2-Y complexes display markedly different behaviour. The plots of molar susceptibility vs., temperature (5-300) K for both the encapsulated complexes along with that of the neat NiL1 are shown in Figure 3C.9. The origin of such radically different behavior of the hybrid system is apparently from the guest nickel complexes, as the host is diamagnetic.^{1, 20} On the other hand, the paramagnetic behaviors of the encapsulated Ni complexes are quite evident.

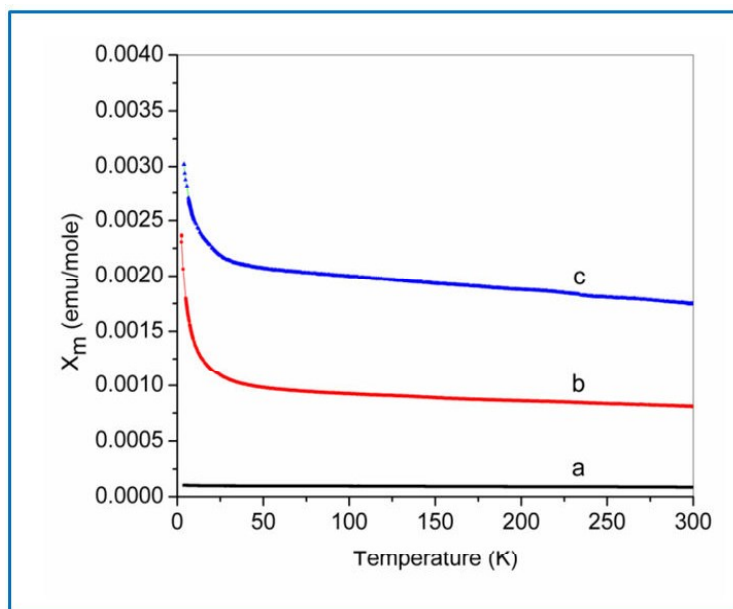


Figure 3C.9: Molar susceptibility vs temperature plots in the range of 4K-300K of (a) NiL1 (b) NiL1-Y and (c) NiL2-Y.

This enhanced paramagnetism must be instigated from the structural deformation of the encapsulated complex where Ni ion experiences an electronic environment different from that of the neat complex, and the non-planar NiN₂O₂ moiety results in an altered ordering of molecular energy levels. As a result, the slightly higher lying excited triplet state becomes comparatively more accessible. This argument is even strongly supported by the theoretical studies and experimentally obtained optical data indicating the fact that encapsulation causes significant reduction of the energy gap between the highest lying metal $d_{x^2-y^2}$ and next highest d_{xy} orbitals. Hence encapsulation enables a considerable fraction of the complex molecules to exist in high energy triplet states and is consequently responsible for the substantial increase in the magnetization of the encapsulated complex.

Comparing the magnetic behaviour of both the encapsulated complexes, we have found that encapsulated NiL2-Y complex has much higher magnetization than the encapsulated NiL1-Y complex establishing the fact that NiL2-Y complex has larger fraction of molecules in higher lying excited triplet states upon encapsulation. It is reasonable, because the bulkier NiL2-Y complex does not fit into the spherical cavity of host and hence suffers from more steric strain to accommodate itself into the cavity thus adopts more distorted geometry than encapsulated NiL1-Y complex.

3C.2.9. Catalytic activity and structural correlation

Catalytic activities of the complex both in free and encapsulated states have been investigated for styrene oxidation reaction using H₂O₂ as oxidant (Table 3C.6, GC chromatogram are shown in Appendix A11 and A15) and Ni-salen system is employed as catalyst. In this reaction, benzaldehyde is identified as major product in each of the cases whereas styrene oxide and phenyl acetaldehyde are the minor products. Nickel Schiff-base complexes are known to be less reactive than other transition metals for the oxidation reactions.^{21, 22} On comparison the percentage conversion data, of both state complexes, neat complexes seems to have high conversion but there is a difference in concentration of active centers (nickel metal) as encapsulated complexes have poor loading level to get maximum free zeolite surface for the reaction so relative reactivity of catalysts has been calculated in term of turnover number, TON. It has been observed that the encapsulated complexes are more selective for benzaldehyde than their corresponding neat state.²¹ NiL1-Y and NiL2-Y complexes in their neat form show comparatively similar reactivity for the oxidation reaction

in terms of Turn Over Number (TON). Interestingly, the NiL2-Y complex shows greater reactivity than NiL1-Y and UV-Vis, magnetic and TD-DFT studies evidently support the greater extent of distortion of planar geometry in NiL2-Y complex. In literature, it has been reported^{23,24} that distortion in planar complexes induces the better reactivity for the oxidation processes because, distorted planar structure induces more electropositive character on the metal, which act as more sensitive site for nucleophilic attack of the reagent. Study of relation in modified functionality and structural behaviour surely provide a new gateway to design the more effective heterogeneous catalyst which will be useful in various industrial processes.

Table 3C.6: Conversion of styrene after 8 hours reaction time with H₂O₂ as oxidant.

S. No	Complexes	% Conversion	TON	Selectivity for bza (%)	Selectivity for so (%)
1	NiL1	13.5	108.64	51.61	48.38
2.	NiL1-Y	4.51	89.6	96.74	3.25
3	NiL2	11.29	100.9	69.34	30.87
4	NiL2-Y	10.23	235	87.73	12.26

Reaction conditions - Styrene: 1.56 g, 15 mmol, H₂O₂: 3.40 g, 30 mmol, acetonitrile 15 ml, temperature 80⁰ C, and catalyst (0.075 g for encapsulated complexes and 0.006 g for neat complexes)TON (turn over number): mole of substrate converted per mole of metal center (encapsulated complexes).

3C.3. CONCLUSION

This section presents detailed characterizations of complexes NiL1 and NiL2 encapsulated in zeolite -Y. The comparative morphological, spectroscopic, magnetic, catalytic and theoretical studies of both complexes have been carried out to explore the effect of the host framework on the guest complexes. XRD pattern, SEM and IR studies have indicated successful formation of the complex inside the zeolite Y cavities. Solid state UV-Visible studies have supported the complex formation in the neat and also in the encapsulated states in zeolite Y, however the d-d transitions of the encapsulated complexes are observed to be blue shifted. Interestingly, observed blue shift in d-d bands is more when compared with NiL1-Y. TD-DFT simulated electronic spectra have supported the experimental observations and indicated that encapsulated complexes are distorted and exist in triplet states. Further the magnetic studies have presented an evident exposure about the distortion in geometry around the Ni

center of encapsulated complexes, because both diamagnetic complexes show paramagnetism whereas NiL2-Y complex shows relatively enhanced magnetism in comparison to NiL1-Y complex, which again proves the effect of substituent groups in the encapsulated complex. Theoretical studies also have indicated a higher magnetic moment for NiL2-Y complex, with respect to NiL1-Y complex, showing good agreement with experimental magnetic behavior. The electronic, magnetic and DFT studies altogether indicate that encapsulation forces the complex to adopt a distorted geometry which drives the Ni atom out of the plane of NiN₂O₂ moiety. This alteration in geometry lowers the energy gap between the triplet and singlet states, which in turn, makes the energetically higher lying triplet state more accessible. Bulkier NiL2-Y complex suffers more space constraint imposed by spherical host cavity, thus, the extent of distortion is higher, driving majority of molecules to the higher energy triplet state, eventually making it more paramagnetic than Ni-salen-Y complex. Enhanced catalytic activity of NiL2-Y complex validates the extent of distortion in adopted geometry of the guest complex as well as offers the evidences about the connection between structural and functional alterations.

REFERENCES

1. W. H. Quayle and J. H. Lunsford, *Inorg. Chem.*, 1982, **21**, 97-103.
2. W. H. Quayle, G. Peeters, G. L. De Roy, E. F. Vansant and J. H. Lunsford, *Inorg. Chem.*, 1982, **21**, 2226-2231.
3. M. Jafarian, M. Rashvand avei, M. Khakali, F. Gobal, S. Rayati and M. G. Mahjani, *J. Phys. Chem. C*, 2012, **116**, 18518-18532.
4. K. K. Bania, D. Bharali, B. Viswanathan and R. C. Deka, *Inorg. Chem.*, 2012, **51**, 1657-1674.
5. Y. Umemura, Y. Minai and T. Tominaga, *J. Phys. Chem. B*, 1999, **103**, 647-652.
6. K. K. Bania and R. C. Deka, *J. Phys. Chem. C*, 2012, **116**, 14295-14310.
7. K. K. Bania, D. Bharali, B. Viswanathan and R. C. Deka, *Inorg. Chem.*, 2012, **51**, 1657-1674.
8. G. Ramanjaneya Reddy, S. Balasubramanian and K. Chennakesavulu, *J. Mater. Chem. A*, 2014, **2**, 15598-15610.
9. A. R. Silva, M. Martins, M. M. A. Freitas, A. Valente, C. Freire, B. de Castro and J. L. Figueiredo, *Microporous Mesoporous Mater.*, 2002, **55**, 275-284.

10. J. G. Dillard and L. T. Taylor, *J. Electron. Spectrosc. Relat. Phenom.*, 1974, **3**, 455-460.
11. L. J. Matienzo, W. E. Swartz and S. O. Grim, *Inorg. Nucl. Chem. Lett.*, 1972, **8**, 1085-1091.
12. K. K. Bania and R. C. Deka, *J. Phys. Chem. C*, 2013, **117**, 11663-11678.
13. M. Asadi, K. A. Jamshid and A. H. Kyanfar, *Inorg. Chim. Acta*, 2007, **360**, 1725-1730.
14. R. Ganesan and B. Viswanathan, *J. Phys. Chem. B*, 2004, **108**, 7102-7114.
15. M. A. Siegler and M. Lutz, *Cryst. Growth Des.*, 2009, **9**, 1194-1200.
16. S. Di Bella, I. Fragala, I. Ledoux, M. A. Diaz-Garcia, P. G. Lacroix and T. J. Marks, *Chem. Mater.*, 1994, **6**, 881-883.
17. A. Boettcher, H. Elias, E. G. Jaeger, H. Langfelderova, M. Mazur, L. Mueller, H. Paulus, P. Pelikan, M. Rudolph and M. Valko, *Inorg. Chem*, 1993, **32**, 4131-4138.
18. H. Yoon and C. J. Burrows, *J. Am. Chem. Soc.*, 1988, **110**, 4087-4089.
19. H.-C. Zhang, W.-S. Huang and L. Pu, *J. Org. Chem.*, 2001, **66**, 481-487.
20. D. N. Stamires and J. Turkevich, *J. Am. Chem. Soc.*, 1964, **86**, 749-757.
21. M. R. Maurya, A. K. Chandrakar and S. Chand, *J. Mol. Catal. A: Chem.*, 2007, **274**, 192-201.
22. M. R. Maurya, S. J. J. Titinchi, S. Chand and I. M. Mishra, *J. Mol. Catal. A: Chem.*, 2002, **180**, 201-209.
23. M. M. Bhadbhade and D. Srinivas, *Inorg. Chem.*, 1993, **32**, 6122-6130.
24. S. Deshpande, D. Srinivas and P. Ratnasamy, *J. Catal.*, 1999, **188**, 261-269.



This document was created with the Win2PDF "print to PDF" printer available at <http://www.win2pdf.com>

This version of Win2PDF 10 is for evaluation and non-commercial use only.

This page will not be added after purchasing Win2PDF.

<http://www.win2pdf.com/purchase/>